Charmonium spectroscopy and mixing with light quark and open charm states from $n_F = 2$ lattice QCD

Gunnar S. Bali,* Sara Collins, and Christian Ehmann

Institut für Theoretische Physik, Universität Regensburg, 93040 Regensburg, Germany
(Received 12 October 2011; published 29 November 2011)

We study the charmonium spectrum including higher spin and gluonic excitations. We determine an upper limit on the mixing of the η_c ground state with light pseudoscalar flavor-singlet mesons and investigate the mixing of charmonia near open charm thresholds with pairs of (excited) D and $\bar{D}$ mesons. For charm and light valence quarks and $n_F = 2$ sea quarks, we employ the nonperturbatively improved Sheikholeslami-Wohlert (clover) action. Excited states are accessed using the variational technique, starting from a basis of suitably optimized operators. For some aspects of this study, the use of improved stochastic all-to-all propagators was essential.

I. INTRODUCTION

During the past decade several new charmonium resonances were discovered, primarily by experiments at the two B-factories but also by CLEO-c and at the Tevatron. With BES-III and the LHC collecting data, possible Super-B factories and the planned PANDA experiment [1] at the FAIR facility, experimental prospects to study these states in more detail and to discover further resonances are very promising. For an overview, see e.g. Refs. [2–8].

Current phenomenological debates focus on the X, Y, and Z resonances that are close to or above open charm thresholds. At least four different frameworks have been suggested to accommodate these states:

(i) $D^{(*)}\bar{D}$ molecules (or deusons) [8–13], composed of a charmed meson $D^{(*)}$ and antimeson $\bar{D}$,

(ii) tetraquark states (or baryonia) [14–18] consisting of diquark-antidiquark pairs, bound by QCD forces,

(iii) $\bar{c}cg$ hybrid (or hermaphrodite) states [19–22] consisting of a charm-anticharm quark pair and additional gluons, and

(iv) a compact $\bar{c}c$ core, bound inside a light meson, hadro-charmonium [23,24].

One example of a molecule or tetraquark candidate is the $X(3872)$. The $Y(4260)$ can at present be accommodated as a hybrid or as a hadro-charmonium state while the $Z^+(4430)$ (if confirmed) could either be a molecule or hadro-charmonium.

The new states also pose novel challenges to lattice simulations. In the case of standard charmonia that can be classified according to a nonrelativistic quark model, the sizeable quark mass $m_c > \Lambda$, where Λ denotes a typical hadronic binding energy, represents the main difficulty: lattice artifacts, that in our case are of $\mathcal{O}[(m_c a)^2]$, are usually not small at currently available lattice spacings a.

In the Υ case the b quark mass can be integrated out and an effective field theory, nonrelativistic QCD (NRQCD), simulated on the lattice [25,26]. However, the charm quark mass m_c is not sufficiently large to allow for this. In this case higher order perturbative or nonperturbative corrections will be sizeable. Therefore, the charm quark needs to be simulated using a relativistic action.

One would expect observables that are very sensitive to the mass m_c to be more strongly affected by lattice artifacts than those that are insensitive to the precise value of this mass. Using effective field theory methods like the Fermilab approach to heavy quarks [27–29] or NRQCD [30] and potential NRQCD [31,32] some insight can be gained into this. For instance, charm quark mass effects on spin-averaged splittings are suppressed by a factor of the squared average relative velocity of the charm quarks v^2. Momentum exchanges $\propto m_c v$ in turn become relevant for the fine structure. Finally, lattice spacing effects on determinations of the mass parameter m_c from the charmonium spectrum are not suppressed by any powers of v. This means that a computation of the spin-averaged spectrum will be less demanding with respect to the continuum limit extrapolation than predictions of the fine structure or of the charm quark mass.

The standard spectroscopy of charmonium states including the continuum limit extrapolation is well understood in the quenched approximation to QCD, see e.g. [33] and references therein, and several new results including sea quark flavors exist, on isotropic lattices [29,34–37] as well as on anisotropic lattices [38] that employ a smaller temporal than spatial resolution $a_t \ll a_s$, to lessen the severity of the scale separation $m_c v > m_c v^2$.

An accurate reproduction of the charmonium fine structure in the continuum limit represents an important test of QCD and of lattice methods. However, taking the continuum limit may be less vital to reproduce qualitative features of loosely bound open charm threshold states that are spatially more extended. In this case, one needs to consider the mixing of states created by two-quark and

---

094506-1

TABLE I.   Identifier (ID), simulation parameters, charm quark κ-value (κ_{charm}), and the number of analyzed effectively statistically independent gauge configurations of our runs.

ID	β	κ	volume	m_{PS}/GeV	a/fm	L/fm	κ_{charm}	N_{conf}
(1)	5.20	0.134 20	$16^3 \times 32$	1.007(2)	0.1145	1.83	0.1163	100
(2)	5.29	0.136 20	$24^3 \times 48$	0.400(1)	0.0770	1.84	0.1245	130
(3)	5.29	0.136 32	$24^3 \times 48$	0.280(1)	0.0767	1.84	0.1244	100

by four-quark operators. Some pioneering studies have already been done, creating states with $\bar{c}q\bar{q}c$ operators [39,40], where q denotes a light quark flavor. However, so far disconnected quark loop diagrams and hence annihilation channels have been neglected. Moreover, lattice studies of the light quark sector, see e.g. Ref. [41], and of string breaking in the static limit [42] teach us that these diagrams and, in particular, mixing between states created by $\bar{c}c$ and $\bar{c}q\bar{q}c$ operators can be important.

Here we will explore methods needed to systematically study charmonium threshold states and apply these to phenomenology. This article is organized as follows. In Sec. II, we will introduce our methods, namely, the gauge ensembles that are being used, the smeared operators that enter our variational analysis, and the all-to-all propagator techniques. In Sec. III, we present results on standard charmonium spectroscopy at a finite lattice spacing, employing two-quark ($\bar{c}c$) creation operators only. This includes higher spin and exotic states and provides us with the improved operators that are needed in Secs. IV and V. In Sec. IV, we investigate the mixing between $\bar{c}c$ and $\bar{q}q$ operators. This will yield an upper limit to the mixing between the flavor-singlet η_c and η mesons that in principle could have an effect on the S-wave fine structure. Finally, in Sec. V, we investigate the contribution of four-quark $\bar{c}c\bar{q}q$ components to radially excited charmonium states, before we conclude in Sec. VI. Some preliminary results were presented at lattice conferences [43–45].

II. SIMULATION DETAILS AND METHODS

A. Gauge configurations

We base our study on $n_{\text{F}} = 2$ configurations of the QCDSF Collaboration generated using the nonperturbatively improved Sheikholeslami-Wohlert (clover) Fermion action [46] and the Wilson gauge action, provided by the QCDSF collaboration. Details can be found in Ref. [47]. The charm quark mass m_c is not sufficiently heavy to allow for a nonrelativistic action with controllable systematics. Therefore, we use the same action for the charm quark as for the light sea/valence quarks, with a well-defined $\mathcal{O}(a)$ improved continuum limit. Note that except for the value of the coefficient $c_{\text{SW}} = c_B = c_E$ the clover action is identical to the version of the Fermilab heavy quark action used, e.g., in Ref. [29] and our results at a finite lattice spacing a may be interpreted accordingly.

We list the ensembles that we employ in Table I, together with an identifier. The lattice spacing is set from the value $r_0 \approx 0.467$ fm. With this choice, the nucleon mass agrees with the experiment when extrapolated to the physical light pseudoscalar mass[1] [47], $m_{\text{PS}} = m_\pi^{\text{phys}}$. The measured values of r_0/a not only depend on the inverse lattice coupling β but also on the mass parameter κ. One can now decide to define a lattice spacing $a(\beta, \kappa)$ or replace this by a chirally extrapolated $a(\beta)$. After performing a chiral extrapolation in the sea quark mass, the results of the two choices obviously should agree for physical observables. Since in this exploratory study we do not attempt such an extrapolation, we decide to set the lattice spacing from the $r_0/a(\beta, \kappa)$ values, as determined at the investigated sea quark κ parameters.

This leaves us with the charm quark mass as the only free parameter, which we set by tuning,

$$m_{1\bar{S}} = \frac{1}{4}(m_{\eta_c} + 3m_{J/\Psi}), \tag{1}$$

to its experimental value of [50], (3067.8 ± 0.4) MeV.

The ensembles (1) and (2) are used to optimize the smearing functions. Our study of mixing between the η_c and the light quark η-meson is performed on (1) where the mass gap between these states is smallest so that one may expect the biggest effect. For the mixing with threshold states, ensemble (3) is used because in this case light D-meson masses are mandatory.

B. The variational method

We extract energy levels E_n from the decay of two-point Green functions in Euclidean time,

---

[1]A recent reanalysis yields somewhat different r_0/a-values [48], in particular, at small quark masses. Here we ignore these developments. Otherwise, we would have to rerun all simulations, readjusting the charm quark mass by -5%, -6% and $+8\%$, on ensembles (1), (2) and (3), respectively. However, most of the charmonium mass is given by $2m_c a$ so that only mass splittings will be affected by such a readjustment. Fortunately, the spin-averaged splittings were found to be rather insensitive to the charm quark mass [49] while the main systematics regarding the fine structure are the unrealistic sea quark content and the missing continuum limit extrapolation.

$$C_{ij}(t) = \langle O_i(t) O_j^{\dagger}(0) \rangle \quad (2)$$

$$= \sum_{n \geq 1} v_i^n v_j^{n*} e^{-E_n t}, \quad (3)$$

where $v_i^n = \langle 0|\hat{O}_i|n\rangle$. In the case of the clover action link reflection positivity is violated and so in principle the above spectral decomposition with positive real energy eigenvalues only becomes valid for sufficiently large Euclidean times. In practice for $t \geq a$, we do not detect any violations. $\hat{O}_i^{\dagger}$ are operators creating states of an isospin I, charm number[2] C, a given momentum and SO(3) $\otimes$ $\mathbb{Z}_2(\otimes\mathbb{Z}_2)$ $J^{P(C)}$ quantum numbers. Note that on the lattice the infinite dimensional O(3) group is broken down to its octahedral O_h subgroup of order 48, with only ten (A_1, A_2, E, T_1, and T_2 times parity) irreducible Bosonic representations. The mapping between the continuum J spins and these O_h spins is given in Tables II and III.

The expectation value Eq. (2) will depend on the time difference between creation and destruction of the state so that for convenience we have set the source time to zero. Obviously, $C_{ij}(t) = C_{ji}^*(t)$ is Hermitian and in our case we will use operators with phases so that it is real and positive definite for $t \geq a$. For large times t the exponential decay of the $C_{ij}(t)$ entries will be governed by the ground state energy E_1, or, for a momentum $\mathbf{p} = \mathbf{0}$, by the ground state mass. Because of the translational invariance of the expectation value, it is sufficient to perform this momentum projection at the sink. We do this for the standard spectroscopy so that we only need to generate point-to-all propagators in this case. Note that we still have the symmetry $C_{ij}(t) = C_{ji}(t)$ in the limit of infinite statistics, however, the statistical errors of $C_{ij}(t)$ and $C_{ji}(t)$ for $i \neq j$ will not be of similar sizes. Replacing off-diagonal elements so that more smearing iterations (see Sec. II C) are applied at the source than at the (momentum-projected) sink reduces the statistical errors.

The convergence in Euclidean time of effective masses,

$$m_{ij,\text{eff}}(t + a/2) = a^{-1} \ln\frac{C_{ij}(t)}{C_{ij}(t + a)}, \quad (4)$$

towards the ground state mass is affected by the quality of the ground state overlap $c_i = |v_i^1|^2 = |\langle 1|\hat{O}_i^{\dagger}|0\rangle|^2$ of the operator $\hat{O}_i$. Having many different such operators at our disposal enables us not only to determine the ground state energy at small t-values where statistical errors are small but also allow us to access excited states, using the variational approach [51–53], also known as the generalized eigenvalue approach.

---

[2]Here we do not consider strangeness, beauty, etc.

TABLE II. Continuum spins that contribute to a given lattice representation.

irrep.	dimension	continuum J
A_1	1	0,4,...
A_2	1	3,...
E	2	2,4,...
T_1	3	1,3,4,...
T_2	3	2,3,4,...

TABLE III. The "inverse" of Table II. Lattice spins that are "embedded" within each continuum spin.

J	O_h rep.	dimensions
0	A_1	1
1	T_1	3
2	E, T_2	2 + 3
3	A_2, T_1, T_2	1 + 3 + 3
4	A_1, E, T_1, T_2	1 + 2 + 3 + 3
...	...	...

We choose a basis of operators $\hat{O}_i$, $i = 1, \ldots, N$, destroying a color singlet state within a given lattice representation. These operators may differ, for example, by their spatial extents or their Fock structures and they are usually not mutually orthogonal. These are then used to construct the correlation matrix Eq. (2). We now solve the symmetrized eigenvalue problem,

$$C^{-1/2}(t_0)C(t)C^{-1/2}(t_0)\psi^n(t, t_0) = \lambda^n(t, t_0)\psi^n(t, t_0). \quad (5)$$

Note that $C^{-1/2}(t_0)C(t)C^{-1/2}(t_0) = 1$ at the normalization time $t = t_0$: everything is expressed relative to the eigenbasis of $C(t_0)$. We order $\lambda^1(t) > \lambda^2(t) > \cdots > \lambda^N(t) > 0$ at large t. To ensure consistency over jackknife samples, in the statistical analysis we also monitor the directions of the eigenvectors. Note that the original nonsymmetrized definition of Ref. [51] yields the same eigenvalues but different, nonorthogonal eigenvectors, $\phi^n(t, t_0) = C^{-(1/2)}(t_0)\psi^n(t, t_0)$,

$$C^{-1}(t_0)C(t)\phi^n(t, t_0) = \lambda^n(t, t_0)\phi^n(t, t_0). \quad (6)$$

If we choose t_0 overly large then excited states will have died out in Euclidean time and the rank of $C(t_0)$ will not be maximal, within the given statistical errors. For t_0 chosen too small, $C(t)$ will receive contributions from more than the N lowest lying states, resulting in unstable eigenvectors and eigenvalues. It can be shown that the eigenvalues behave like [53],

$$\lambda^n(t, t_0) \propto e^{-(t-t_0)E_n}[1 + \mathcal{O}(e^{-(t-t_0)\Delta E_n})], \quad (7)$$

where ΔE_n is the energy difference between the energy of the first state not contained in the operator basis,[3] E_{N+1} and E_n. The correction factor arises from the finite dimensionality and nonorthogonality of the operator basis. Ideally one will aim at a set of operators that dominantly couple to the first N states and that are as orthogonal as possible to each other. The eigenvectors, up to the rotation and the change in the normalization of Eq. (5), approach their physical counterparts v^n of Eq. (3) too, with similar exponential corrections in Euclidean time [53].

From the eigenvalues we can also define effective energy levels, or, for $\mathbf{p} = \mathbf{0}$, masses,

$$m_{n,\mathrm{eff}}^{t_0}(t + a/2) = a^{-1} \ln \frac{\lambda^n(t, t_0)}{\lambda^n(t + a, t_0)}, \qquad (8)$$

that, for sufficiently large t_0 and $t > t_0$, should exhibit plateaus which we then fit to a constant to obtain the masses m_n.

C. Fermion field smearing

The variational method is the central tool of our analysis. It needs to be supplied with suitable building blocks in terms of operators, from which good approximations of the physical eigenstates can be obtained. The wave functions of physical eigenstates will not be ultralocal objects and spatially extended interpolators need to be considered. We generate such extended operators by applying Wuppertal smearing [54] to a Fermion field ψ,

$$\psi_x^{(n)} = \frac{1}{1 + 6\delta} \left(\psi_x^{(n-1)} + \delta \sum_{j=\pm 1}^{\pm 3} \bar{U}_{x,j} \psi_{x+a\hat{\jmath}}^{(n-1)} \right). \qquad (9)$$

$n = 1, \ldots, n_{\mathrm{wup}}$ counts the iteration number and $\delta > 0$ is a free parameter. The (arbitrary) normalization convention is chosen to avoid numerical overflows for large iteration counts n_{wup}. $\bar{U}_{x,j}$ is a gauge covariant transporter, connecting the lattice point x with its spatial neighbor in the j-direction, $x + a\hat{\jmath}$, for instance a gauge link $U_{x,j}$. In our implementation, we used APE smeared [55] links for $\bar{U}_{x,j}$; see Sec. II D below. Note that the Wuppertal smearing operator is gauge covariant. It transforms as a singlet under O_h, parity and charge transformations, it is Hermitian, translationally invariant and spin-diagonal.

We can rewrite the above equation by defining a covariant spatial lattice Laplacian,

$$a^2(\nabla^2\psi)_x = -6\psi_x + \sum_{j=\pm 1}^{\pm 3} \bar{U}_{x,j} \psi_{x+a\hat{\jmath}}, \qquad (10)$$

---

[3]At least to first order in perturbation theory. To second order states with energies $\leq E_n$ can contribute as well, at $t \gg t_0$. In Ref. [53], it has been shown that these effects are negligible for $t \lesssim 2t_0$. In general the maximum admissible value of t at a given t_0 depends on the underlying spectrum and on the basis of trial wave functions used.

to obtain,

$$\psi^{(n)} = \psi^{(n-1)} + \frac{\delta}{1 + 6\delta} a^2 \nabla^2 \psi^{(n-1)}. \qquad (11)$$

We introduce a fictitious time $t = n_{\mathrm{wup}} \Delta t$,

$$\frac{\partial \psi(t)}{\partial t} \approx \frac{\psi(t + \Delta t) - \psi(t)}{\Delta t} = k \frac{a^2}{\Delta t} \nabla^2 \psi(t), \qquad (12)$$

where

$$k = \frac{\delta}{1 + 6\delta}. \qquad (13)$$

The diffusion equation Eq. (12) is formally solved by,

$$\psi(t) \approx e^{k(t/\Delta t)a^2 \nabla^2} \psi(0). \qquad (14)$$

Starting from a δ-source $\psi_x(0) = \delta_{x0}$ on a free configuration $U_{x,j} = 1$, this results in a Gauss packet with the root mean square (rms) radius of $\psi^\dagger \psi$,

$$\frac{\Delta r}{a} = 3\sqrt{kt/\Delta t} = 3\sqrt{\frac{\delta}{1 + 6\delta}} \sqrt{n_{\mathrm{wup}}}. \qquad (15)$$

The diffusion speed is maximal for $\delta \to \infty$ ($k \to 1/6$) while the resulting wave function is more continuumlike for $\delta \to 0$ ($k \to 0$). As a compromise we choose $\delta = 0.3$ ($k \approx 1/9.3$).

By adjusting n_{wup}, we can control the overlap of our trial wave functions with the physical states. Using a point operator will lead to an effective mass with a significant curvature at small Euclidean times. A few iterations of smearing can help to flatten this out, suppressing the overlap with high excitations that have many nodes in their wave functions. Our strategy is to use an operator basis with a point operator that couples well to excited states, a narrow operator that couples well to the ground state, and one operator that is somewhat wider.
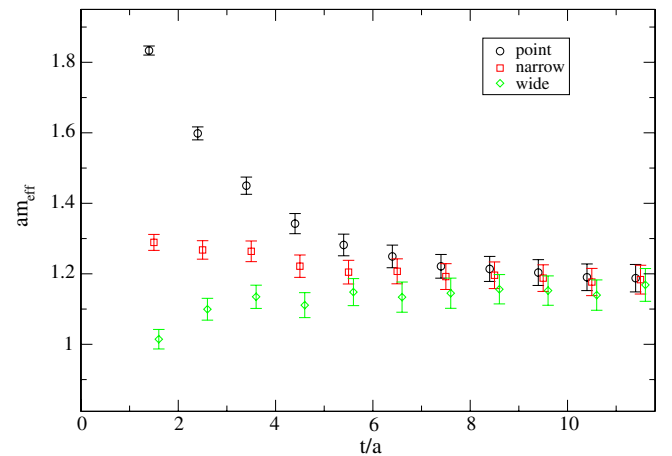

FIG. 1 (color online). Effective masses of correlation functions between a point source and point, narrow and wide smeared sinks.
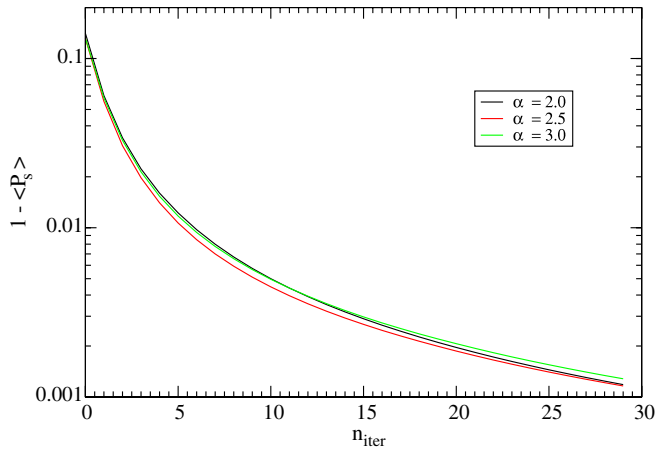
FIG. 2 (color online). Deviations of the average spatial pla-quette from unity, against the number of APE smearing iterations Eq. (16) on a lattice of ensemble (1) for different α values.

In Fig. 1, we display effective masses for the pseudo-scalar charmonium state, with a $\bar{c}\gamma_5 c$ point source and with a point as well as with smeared sinks, on ensemble (2); see Table I. Note that since creation and destruction operators differ, in the smeared cases the effective masses do not need to decrease monotonically. We employed $n_{\text{wup}} = 20$ and 80 smearing iterations for the narrow and wide sinks, respectively. Note that we smeared both quark and anti-quark fields so that the effective radius of the charmonium creation operator is by a factor $\sqrt{2}$ bigger than the expectation in Eq. (15).

D. Gauge field smearing

It was already suggested in Ref. [54] to replace the gauge links within Eq. (9) by other covariant transporters $\bar{U}_{x,j}$, that depend on spatial links within the given time slice. The ground state wave function is smooth and so we may wish to reduce the gauge field fluctuations as well, to enhance the overlap with low lying states. Following Ref. [42], we employ spatial APE smearing [55] to the gauge links that enter the Wuppertal smearing, iteratively replacing a link by a linear combination of the link and the sum of the four surrounding spatial staples,

$$V_{x,i}^{(n)} = U_{x,i}^{(n-1)} + \alpha \sum_{|j| \neq i} U_{x,j}^{(n-1)} U_{x+a\hat{j},i}^{(n-1)} U_{x+a\hat{i},j}^{(n-1)\dagger},$$

$$U_{x,i}^{(n)} = P_{\text{SU}(3)} V_{x,i}^{(n)}. \tag{16}$$

$\alpha > 0$ is a weight factor and $P_{\text{SU}(3)} A$ projects A onto $U \in$ SU(3) so that $\text{Re}\,\text{Tr}(UA^\dagger)$ is maximal. This procedure somewhat deviates from the definition of Ref. [42] but also preserves gauge covariance.

The spatial plaquette $\langle P_s \rangle$ measures the curvature of the gauge fields. Maximizing this means a smoother gauge background. In Fig. 2, $1 - \langle P_s \rangle$ is plotted against the number of APE smearing iterations on lattices of ensemble (1) (see Table I) for three values of α. The approach to unity depends very little on the gauge configuration or on the gauge ensemble that we use. We decide to terminate the APE smearing after $n_{\text{ape}} = 15$ iterations, using $\alpha = 2.5$, as a compromise between gauge field smoothness and the computer time spent.

APE smearing brings the links close to unity while preserving the gauge covariance of the Wuppertal smear-ing. This means that Eq. (15), which is valid for $\Delta r \gg a$ on trivial gauge fields, is satisfied with good accuracy. In Fig. 3, we display a color component after applying $n_{\text{wup}} = 100$ smearing iterations to a δ-source in Coulomb gauge, without and with APE smearing. Indeed, the trial wave
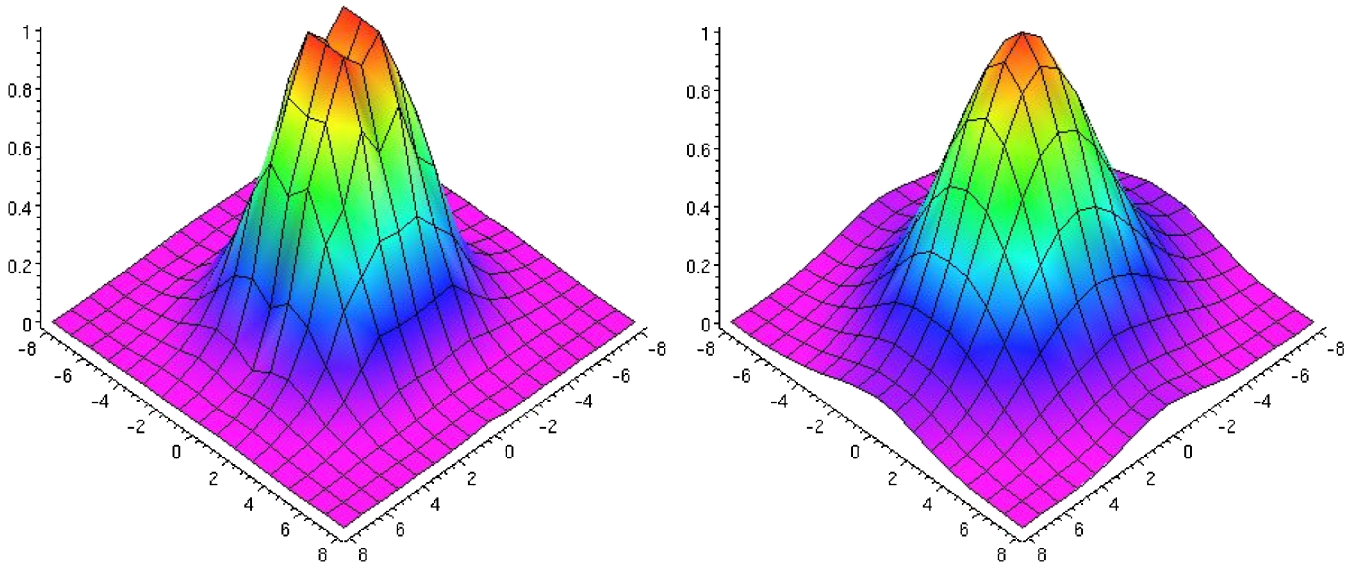

FIG. 3 (color online). The Wuppertal smearing function ($n_{\text{wup}} = 100$, $\delta = 0.3$) with the original gauge links as parallel transporters (left) and with APE smeared transporters (right).

function looks smoother and moreover, we obtain the rms radius expected from Eq. (15).

Note that the APE smeared fields are only used to improve the operators but not to propagate the quarks. The inversions of the lattice Dirac operator are performed on the original gauge configurations.

E. All-to-all propagators

We first introduce the stochastic method to estimate all-to-all propagators. We then describe the improvement methods that we employ, namely, staggered spin partitioning (SSP) [44], the hopping parameter expansion (HPE) [56], and recursive noise subtraction (RNS) [44]. We finally investigate the efficiency of combinations of these methods for a realistic example. Note that on top of this we also employ the truncated solver method (TSM) [57,58]; see also Ref. [59], that turns out to be beneficial even for masses as heavy as that of the charm quark. We restrict its use to light quark propagators, though.

1. Definitions and basics

We denote the improved lattice Wilson-Dirac operator by,

$$M = \frac{1}{2\kappa}(1 - \kappa D). \tag{17}$$

This will depend on the quark mass through κ. For each of the 12δ-sources $|0, \alpha, a\rangle$ at spacetime position 0, spin α and color a, we can compute solutions $|s^{0,\alpha,a}\rangle$ of the linear systems,

$$M|s^{0,\alpha,a}\rangle = |0, \alpha, a\rangle. \tag{18}$$

This defines the point-to-all propagator,

$$S(x|0)^{ba}_{\beta\alpha} = s^{0,\alpha,a}(x, \beta, b). \tag{19}$$

Because of translational invariance of expectation values, point-to-all propagators are often sufficient to calculate hadronic two-point Green functions. However, if one had all-to-all propagators at one's disposal, one would gain statistics from self-averaging over different source points. Moreover, some Wick contractions inevitably lead to diagrams containing disconnected quark loops whose evaluations require more than a few source points. Solving the 12 equations Eq. (19) for all V lattice points (in our case, $V = 131\,072$ and $663\,552$) instead of for a single $x_0 = 0$ is prohibitive in terms of computer time and memory.

However, we encounter statistical errors anyway from the path integral importance sampling in the calculation of expectation values. Hence, it is sufficient to aim at an unbiased estimate, which can be obtained using stochastic methods [60,61]. We introduce the following notation,

$$\bar{A} = \bar{A}^N := \frac{1}{N}\sum_{j=1}^{N} A^j, \tag{20}$$

and define random noise vectors $|\eta^j\rangle$, $j = 1, \ldots, N$ with components,

$$\eta^j(x, \alpha, a) = \langle x, \alpha, a|\eta^j\rangle \in \frac{1}{\sqrt{2}}(\mathbb{Z}_2 \otimes i\mathbb{Z}_2). \tag{21}$$

This complex $\mathbb{Z}_2$ noise has the properties,

$$|\bar{\eta}\rangle^N = \mathcal{O}(1/\sqrt{N}), \tag{22}$$

$$\overline{|\eta\rangle\langle\eta|}^N = 1 + \mathcal{O}(1/\sqrt{N}). \tag{23}$$

By solving,

$$M|s^j\rangle = |\eta^j\rangle, \tag{24}$$

for $|s^j\rangle$, $j = 1, \ldots, N$, one can construct an unbiased estimate; see Eq. (23),

$$M_E^{-1} := \overline{|s\rangle\langle\eta|} \approx M^{-1}, \tag{25}$$

$$M_E^{-1} = M^{-1} - M^{-1}\left(1 - \overline{|\eta\rangle\langle\eta|}\right). \tag{26}$$

$1 - \overline{|\eta\rangle\langle\eta|}$ is an off-diagonal matrix with entries of $\mathcal{O}(1/\sqrt{N})$. Hence, the difference between the approximation of Eq. (25) above and the exact result reduces like $1/\sqrt{N}$. When averaging over n_{conf} gauge configuration, the additional stochastic errors of an estimated observable reduce like $1/\sqrt{Nn_{\mathrm{conf}}}$ since the estimate is unbiased. One would like to achieve some sort of balance where this stochastic error becomes smaller than the unavoidable gauge error $\propto 1/\sqrt{n_{\mathrm{conf}}}$ from averaging over the configurations. Since the ratio of these sources of errors is independent of n_{conf}, once this is large enough for the central limit theorem to hold, this optimization can be performed on a small number of configurations. Depending on the observable, a large number of estimates N may be required, unless the difference Eq. (26) can be reduced. Indeed, many methods of improving estimates exist, see, e.g. [58] and references therein.

Below we introduce the improvement methods that we use in this article.

2. Staggered spin partitioning

One source of large uncertainties of the naïve estimate is that the noise source vectors have entries on all lattice sites. The site, where the propagator ends, is surrounded by components of the source vector that may not contribute to the signal but that will contribute to the noise. To see this more clearly, consider the estimation of a propagator Eqs. (18) and (19) connecting the point x with the point y [see also Eq. (26)],

$$S_E(y|x)^{ba}_{\beta\alpha} = S(y|x)^{ba}_{\beta\alpha} - \sum_{z,\gamma,c} S(y|z)^{bc}_{\beta\gamma}\left[1 - \overline{|\eta\rangle\langle\eta|}\right](z|x)^{ca}_{\gamma\alpha}, \tag{27}$$
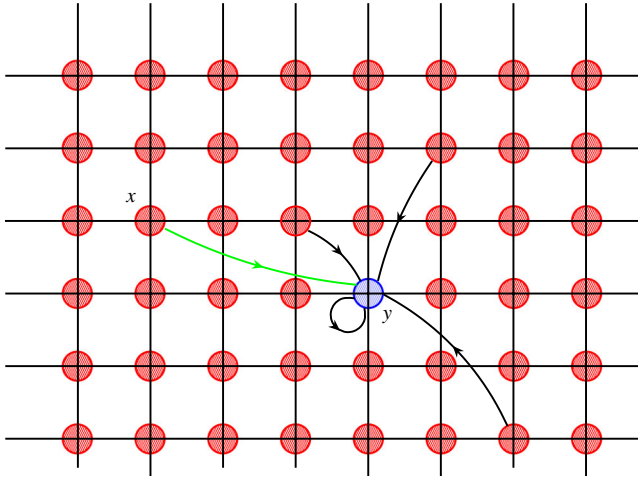
FIG. 4 (color online). Two-dimensional sketch of a global noise source. For the propagator from x to y, only the green (light) line contributes to the signal; the black ones contribute to the noise.

where only entries with either $z \neq x$, $\gamma \neq \alpha$ or $c \neq a$ give nonvanishing contributions to the noise sum, see Fig. 4.

Since signals decrease exponentially with Euclidean distances,

$$||S(y|z)|| \sim e^{-|y-z|/\xi}, \qquad (28)$$

the source components located in the nearest neighborhood of y contribute most to the noise[4] and thus it is desirable to reduce or to remove these terms entirely. Likewise, contributions that are off-diagonal in spin or color at y should be avoided. A brute force way of achieving this is by "partitioning" [62–64]. For the special case of spin partitioning, this is also known as the spin explicit method [63].

Partitioning amounts to decomposing $\mathcal{R} = V \otimes$ colour $\otimes$ spin into m subspaces $\mathcal{R}_j$: $\mathcal{R} = \oplus_{j=1}^{m} \mathcal{R}_j$. One can set the source vectors $|\eta_{|j}\rangle$ to zero, outside of the subspace $\mathcal{R}_j$, and label the corresponding solutions as $|s_{|j}^i\rangle$. The estimate of the all-to-all propagator is then given by the sum,

$$M_E^{-1} = \sum_{j=1}^{m} \overline{|s_{|j}\rangle\langle\eta_{|j}|}. \qquad (29)$$

Clearly, this results in an m-fold increase of the total number of solver applications. If the stochastic noise reduction exceeds a factor $1/\sqrt{m}$, then this computational overhead is justified.

Here we utilize spin and color partitioning. So far within each spin partitioning set the same spinor component was

---

[4]This heuristic argument is over-simplistic since S is not a gauge invariant quantity. However, similar calculations can be performed for errors of physical observables, with the same result.

dialed on every lattice site; see Fig. 5. Depending on the observable, however, it may be favorable to alter the component to be filled within a specific set as a function of the spacetime position. For heavy quarks, the coupling between the upper and the lower two components of the Dirac spinor is small. One may exploit this by separating in spacetime components that couple strongly, only allowing for weakly coupled components to share a link. We call such nontrivial spin partitioning schemes staggered spin partitioning (SSP) [44]. In Fig. 6, we sketch two SSP versions, off-diagonal SSP (odSSP) and off-block-diagonal SSP (obdSSP). Figure 7 illustrates the coupling strengths between the four spinor components. Red lines indicate
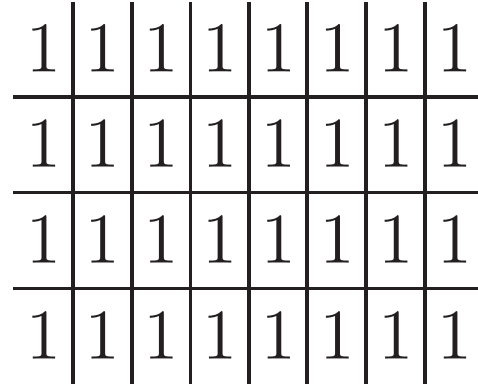

FIG. 5. Two-dimensional schematic sketch of standard spin partitioning. The numbers indicate the spinor component filled at the specific lattice site for set 1 (out of 4).
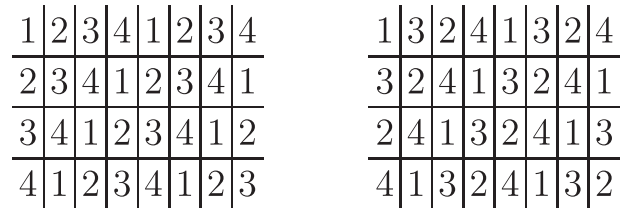

FIG. 6. Two-dimensional schematic sketch of odSSP (left) and obdSSP (right). The numbers indicate the spinor component filled at the specific lattice site for set 1 (out of 4).
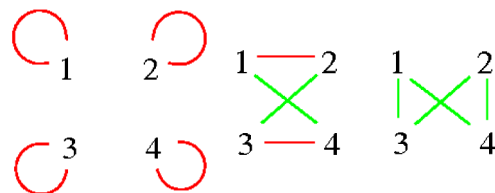

FIG. 7 (color online). The coupling strengths between the spinor components of standard (left), off-diagonal (center), and off-block-diagonal (right) spin partitionings. Red (dark) indicates a strong (i.e. nearest neighbor) coupling, green (light) a weak (i.e. next-to-nearest neighbor) coupling.

nearest neighbors (strong coupling) and green lines next-to-nearest neighbors (weak coupling).

The obdSSP scheme should be particularly well-suited to heavy quarks. However, this also depends on the discretization of the Dirac matrix and on the Γ- and derivative-structure of the creation operators. Hence, predicting the efficiency of a specific scheme is difficult. An object frequently appearing in this work is the pseudoscalar loop $\mathrm{Tr}(\gamma_5 M^{-1})$. In our spinor representation, γ_5 is diagonal so that the naïve picture presented above may apply. For other, nondiagonal Γ-structures, different SSP schemes may be more effective. The picture becomes further obscured since within all the partitioning schemes there will be residual couplings between different color components on the same site too. Fortunately, these terms are suppressed by the fact that $S(y|y)$ will be quite color-diagonal, in particular, in the heavy quark limit. We also investigate combinations of (S)SP and color partitioning.

3. Hopping parameter expansion

We have seen above that stochastic noise components that are close to the diagonal of the inverse Fermionic matrix M^{-1} are accompanied by larger amplitudes than terms that are far off the diagonal. Therefore, the cancellation of near-diagonal noise requires a comparatively larger number of estimates. The HPE noise subtraction [56] is based on the observation that one can expand, see Eq. (17),

$$M^{-1} = 2\kappa \sum_{i=0}^{\infty} (\kappa D)^i = 2\kappa \sum_{i=0}^{k-1} (\kappa D)^i + (\kappa D)^k M^{-1}, \quad (30)$$

where $k \geq 1$. For distances between source and sink that are composed of more than k links, the first term on the right-hand side does not contribute since D only connects nearest spacetime neighbors. Therefore, $M_{xy}^{-1} = [(\kappa D)^k M^{-1}]_{xy}$ for sufficiently large source and sink separations. However, their estimates will differ, $M_{E,xy}^{-1} \neq [(\kappa D)^k M_E^{-1}]_{xy}$. The variance of the latter estimate of M_{xy}^{-1} will be reduced since less noise terms contribute and, in particular, the dominant sources of noise have been removed. This was for instance exploited in Refs. [42,65].

We illustrate the HPE technique in Fig. 8: one application of κD reduces the blue contributions, two applications the green ones, three applications the yellow ones, and so forth. However, note that unlike in the case of partitioning, these are not completely removed since they can propagate along a longer path to reach the sink, weakening their effect. It is self-evident that the HPE will be particularly effective for heavy quarks.

Here we also study closed loops, i.e. $x = y$. Obviously, only even powers of D contribute to $\mathrm{Tr}(M^{-1}\Gamma)$, where $\Gamma \in \{1, \gamma_\mu, \sigma_{\mu\nu}, \gamma_\mu \gamma_5, \gamma_5\}$. We can write, $\mathrm{Tr}(M^{-1}\Gamma) = \kappa^k \mathrm{Tr}(D^k M^{-1}\Gamma)$ for $k \leq k_{\max}$. For $\Gamma = \gamma_5$ and $\Gamma = \gamma_i$ for the clover action, $k_{\max} = 2$. Moreover, the lowest nonvanishing terms have been calculated analytically and can be
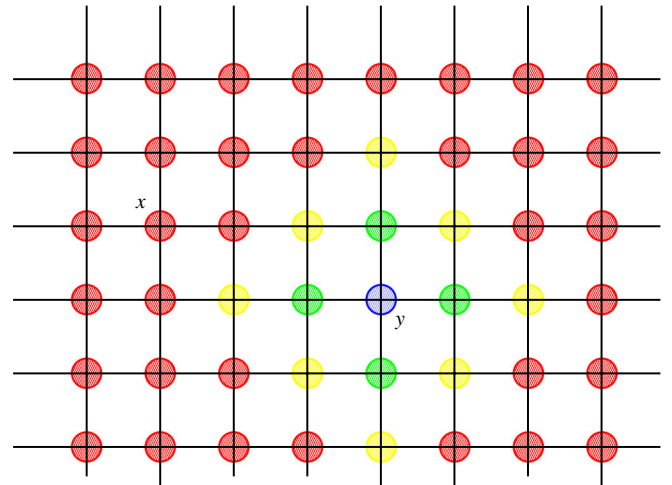

FIG. 8 (color online). Two-dimensional sketch of the effect of HPE. y indicates the sink and x an arbitrary source site. One application of κD reduces the blue (dark), two applications the green (medium dark), and three applications the yellow (light) contributions to the noise.

computed and corrected for exactly (unbiased noise subtraction) [56,66–68]. Here we do not attempt to do this but we restrict ourselves to $k = 2$ instead.

The HPE comes with very little computational overhead and, unlike in the case of partitioning, no additional solves are required.

4. Recursive noise subtraction

Within the RNS method [44], the off-diagonal terms of Eq. (26) are estimated and subsequently corrected for,

$$M^{-1} = \overline{|s\rangle\langle\eta|} + M^{-1}\left(1 - \overline{|\eta\rangle\langle\eta|}\right)$$
$$\approx \overline{|s\rangle\langle\eta|} + \overline{|s\rangle\langle\eta|}\left(1 - \overline{|\eta\rangle\langle\eta|}\right), \quad (31)$$

in the hope to arrive at an improved estimate. The second term of the last line of the above equation involves additional inner products $\langle\eta_i|\eta_j\rangle$. For $i \neq j$, these fluctuate randomly, but we sum over $12V \gg N^2$ such terms, where N is the number of estimates. Clearly, the procedure can only work if this inner product is taken over a smaller subspace. Therefore, we compute the random matrix $\overline{|\eta\rangle\langle\eta|}$ only in the spin- color subspace, setting all elements connecting different sites to zero.

In Fig. 9, we display the correlation between the two terms of Eq. (31) for the pseudoscalar loop $\mathrm{Tr}(M^{-1}\gamma_5)$. Since the two quantities are anticorrelated, adding them together reduces the statistical error. So far we have assumed the coefficient of the second term of Eq. (31) to be unity. However, realizing that this term is an unbiased estimate of zero, one can generalize this method, e.g. by allowing for an adjustable coefficient. Moreover, different terms involving powers of $1 - \overline{|\eta\rangle\langle\eta|}$ and/or a different
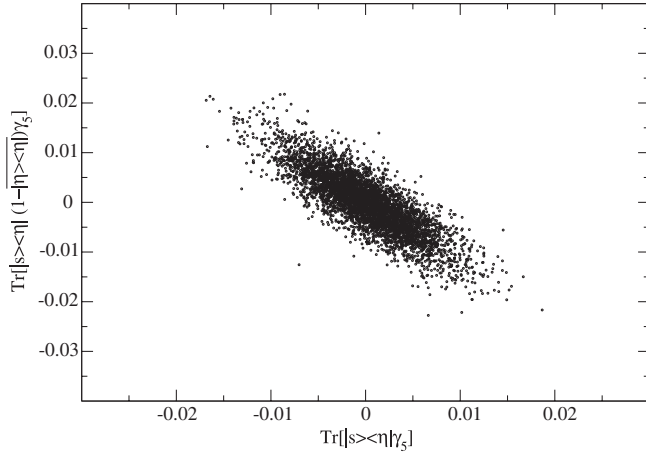
FIG. 9. Scatter plot for the RNS; see Eq. (31) for the pseudoscalar loop.

subspace where this matrix assumes nontrivial values could be implemented. However, we have not explored these possibilities any further.

5. Comparison of methods

We will apply the methods presented so far, to calculate disconnected quark loop contributions to the charmonium spectroscopy. An important example is the correlation of two zero-momentum-projected disconnected loops, e.g.,

$$\sum_{x,\mathbf{y}} \langle \text{Tr}[(\Phi M^{-1}\Phi)_{yy}\gamma_5]\text{Tr}[(\Phi M^{-1}\Phi)_{xx}\gamma_5]\rangle, \qquad (32)$$

for the η_c mass where $y_4 = x_4 + t$. $\Phi = \Phi^\dagger$ denotes a Wuppertal smearing function and the traces are over spin and color. Note that the above traces are real, due to $M^\dagger = \gamma_5 M\gamma_5$. We also remark that we used two separate sets of noise vectors to estimate the two traces, as one has to do. To compare the methods, we choose $t = a$ and $n_{\text{wup}} = 10$ on ensemble (1).

The improvements in terms of the real computer time spent to achieve the same stochastic error are displayed in Table IV for different combinations of methods. All over-

TABLE IV. Gain factors of the noise reduction methods tested for the pseudoscalar disconnected correlator Eq. (32) at the charm quark mass. k denotes the number of κD applications.

k	0	2
no partitioning	1	2.89
spin	1.43	6.32
color	1.80	5.06
spin + color	2.52	10.24
odSSP	2.30	5.42
obdSSP	1.97	7.16
obdSSP + color	3.63	11.80
RNS	1.87	5.44

heads are included, except for the (negligible) cost of the two κD applications. k denotes the power of κD applied to the solution vector. The biggest net gain factor amounts to almost 12. Based on these numbers, we decide to use the obdSSP and color partitioning, together with the HPE for this type of diagram.

III. THE SPECTRUM

In this section, we calculate the spectrum created by $\bar{c}c$ quark bilinears, neglecting charm quark annihilation and light quark creation diagrams. We first discuss our operator basis and then the spectroscopy results. The variational method also reveals information about the spatial structure of the underlying states. We will discuss this as well as the mixing between S- and D-wave operators in the $J^{PC} = 1^{--}$ vector channel.

A. Extraction of masses

The operators that we employ to create the charmonium states are based on Ref. [69]. We restrict ourselves to the subset of these operators for which we are able to obtain meaningful signals. These are displayed in Table V, together with their irreducible lattice representations and the corresponding lowest continuum spin assignments; see Table II. These assignments are, of course, not unique. For instance, a radial T_1 excitation can, in the continuum limit, very well correspond to $J = 3$ or $J = 4$; see Table III. We label the operators by the names of the corresponding isovector mesons (which in nature are no charge eigenstates) since we are most familiar with these.

Note that in the nonrelativistic quark model,

$$P = (-)^{L+1}, \qquad C = (-)^{L+S}, \qquad (33)$$

where $S \in \{0, 1\}$ and $J \in \{L + S, L, |L - S|\}$. The states that cannot be accommodated in this way, namely $0^{--}, 0^{+-}, 1^{-+}, 2^{+-}, 3^{-+}, \ldots$, are commonly referred to

TABLE V. Quark bilinears that we use ($s_{ijk} = |\epsilon_{ijk}|$, also see Eq. (34)).

name	O_h repr.	J^{PC}	state	operator
π	A_1	0^{-+}	η_c	γ_5
ρ	T_1	1^{--}	J/Ψ	γ_i
b_1	T_1	1^{+-}	h_c	$\gamma_i\gamma_j$
a_0	A_1	0^{++}	χ_{c0}	1
a_1	T_1	1^{++}	χ_{c1}	$\gamma_5\gamma_i$
$(\rho \times \nabla)_{T_2}$	T_2	2^{++}	χ_{c2}	$s_{ijk}\gamma_j\nabla_k$
$(\pi \times D)_{T_2}$	T_2	2^{-+}		$\gamma_4\gamma_5 D_i$
$(a_1 \times \nabla)_{T_2}$	T_2	2^{--}		$\gamma_5 s_{ijk}\gamma_j\nabla_k$
$(\rho \times D)_{A_2}$	A_2	3^{--}		$\gamma_i D_i$
$(b_1 \times D)_{A_2}$	A_2	3^{+-}		$\gamma_4\gamma_5\gamma_i D_i$
$(a_1 \times D)_{A_2}$	A_2	3^{++}		$\gamma_5\gamma_i D_i$
$(a_1 \times B)_{T_2}$	T_2	2^{+-}	exotic	$\gamma_5 s_{ijk}\gamma_j B_k$
$(b_1 \times \nabla)_{T_1}$	T_1	1^{-+}	exotic	$\gamma_4\gamma_5\epsilon_{ijk}\gamma_j\nabla_k$

as "spin-exotic" states. As one can see from the 1^{-+} example of Table V, these exotic states do not need to be tetraquarks/molecules or hybrid mesons. With relativistic quarks, local bilinears are not restricted to 0^{-+} and 1^{--} anymore but e.g. 1^{+-} can be created with $L = 0$. In this case, the "exotic" 1^{-+} state is merely a 1^{+-} quark bilinear in a P-wave. We also remark that, in QCD with finite quark masses, L is not a good quantum number. However, it may still provide us with some guidance if the quarks are heavy. We will address this issue in Sec. III D below.

In Table V, ∇ represents a covariant spatial derivative and D and B the symmetrized and antisymmetrized combinations,

$$D_i = s_{ijk}\nabla_j\nabla_k, \qquad B_i = \epsilon_{ijk}\nabla_j\nabla_k, \qquad (34)$$

with $s_{ijk} = |\epsilon_{ijk}|$, and we sum over j and k. All operators containing a covariant derivative implicitly also include gluonic contributions but then any P- or D-wave will include derivatives and one would hardly call these hybrid mesons. However, the B_i-operators not only contain the vector potential, but they are proportional to components of the field strength tensor itself. This is as close to a valence gluon as one can get. A strong coupling of a physical state to this operator may then indicate a large hybrid meson content. The 1^{-+} charmonium is considered a prime hybrid candidate. However, we find the operators

$\epsilon_{ijk}\gamma_j B_k$ (T_1 representation, not listed in the Table) to be very noisy, with no compelling evidence of a coupling to the ground state created by $b_1 \times \nabla$.

For each operator listed in the table, we construct a three-by-three cross-correlator matrix, see Sec. II B, with different smearing levels, see Sec. II C. We apply the same smearing to quark and antiquark. The smearing parameters have been optimized for several states as described in Sec. II C, so that point-smeared effective masses are relatively constant for the narrow operator and approach their asymptotic values from below for the wide operator. We only consider the two lowest lying masses reliable since the highest state contained in the basis may be polluted by even higher excitations. In Ref. [70], a similar approach was used to calculate the spectra of excited states in the quenched approximation.

B. Discussion of the results

We display effective masses for ensemble (1) (see Table I), obtained after diagonalizing the correlation matrices at the normalization time t_0; see Eq. (5), for some of the channels in Fig. 10. Only the lowest two masses are fitted and the fit ranges are indicated by the blue lines. The extracted mass values, together with these fit ranges, are displayed in Table VI. In this table, we also assign the lowest possible continuum spin to each channel. Note,
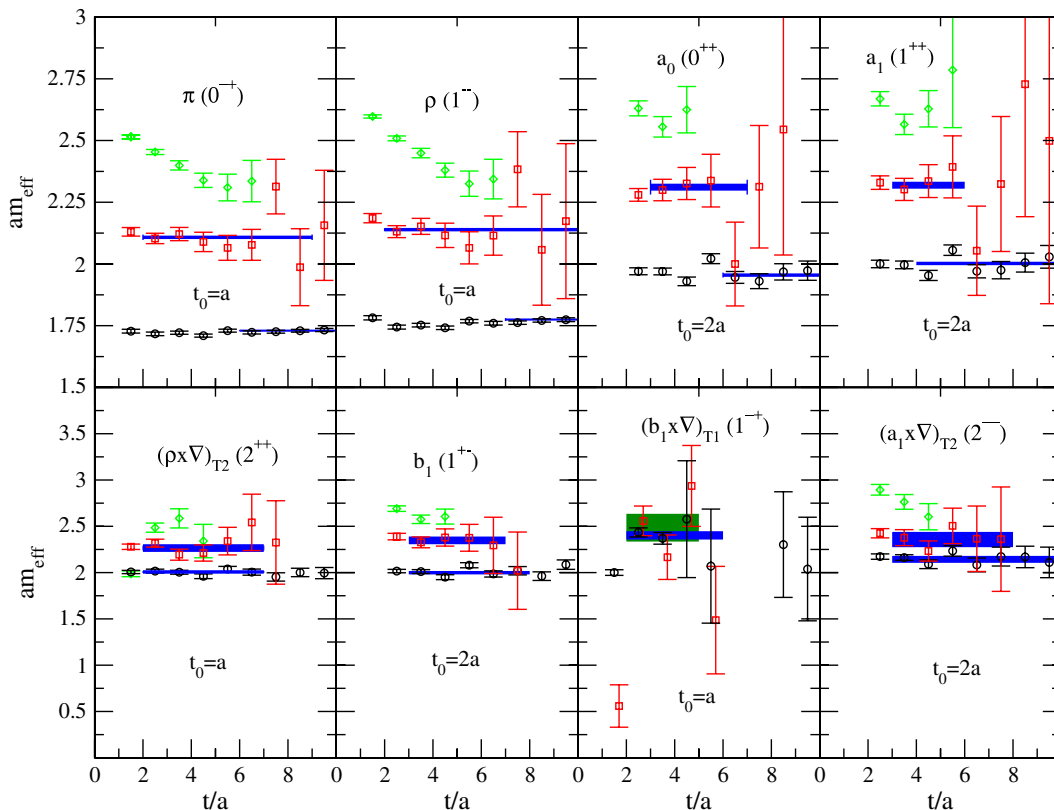

FIG. 10 (color online). Effective masses for some operators of Table V obtained on ensemble (1). The fit ranges and errors are indicated by horizontal lines. The t_0 values (in lattice units) refer to the respective normalization times Eq. (5).

TABLE VI.   Fitted masses obtained on ensemble 1 for the first two eigenvalues in each channel. The normalization time t_0 and the corresponding fit ranges are also given. The errors are only statistical and we give the lowest continuum J^{PC} from which the lattice representation can be subduced.

operator	J^{PC}	t_0/a	$m_1/$ MeV	range	$m_2/$MeV	range
π	0^{-+}	1	2993 (4)	5–12	3645 (19)	1–8
ρ	1^{--}	1	3070 (6)	7–12	3699 (24)	1–7
b_1	1^{+-}	2	3457 (22)	2–7	4060 (65)	1–5
a_0	0^{++}	2	3381 (19)	4–12	3996 (48)	1–5
a_1	1^{++}	2	3462 (20)	3–11	4011 (52)	1–5
$(\rho \times \nabla)_{T_2}$	2^{++}	1	3471 (19)	1–6	3917 (46)	1–6
$(\pi \times D)_{T_2}$	2^{-+}	1	3756 (32)	1–9	3995(141)	1–6
$(a_1 \times \nabla)_{T_2}$	2^{--}	2	3706 (27)	1–10	4076 (83)	1–6
$(\rho \times D)_{A_2}$	3^{--}	1	3782 (35)	1–8	4815 (92)	1–6
$(b1 \times D)_{A_2}$	3^{+-}	1	3995 (50)	2–6	5365 (76)	1–3
$(a_1 \times D)_{A_2}$	3^{++}	2	3993 (54)	1–5	5008(287)	1–4
$(b_1 \times \nabla)_{T_1}$	1^{-+}	1	4154 (54)	1–5	4297(181)	1–4
$(a1 \times B)_{T_2}$	2^{+-}	1	4614(220)	1–9	4643(254)	1–8

however, that radial excitations of both $J = 1$ ($= T_1$) and $J = 2$ ($= T_2$) states could in principle correspond to $J = 3$. In particular, this possibility cannot be excluded for the excitations of the T_1 states that we have labeled as 1^{+-} and 1^{++} and for the T_2 state labeled as 2^{++}.

The ground states and first excitations of the standard S- and P-wave states η_c, J/Ψ, h_c, and χ_{cJ} exhibit good signals and stable plateaus. The effective masses of higher spin states are naturally noisier and thus complicate the fits.

A particularly interesting channel is the 1^{-+}. Although this is a spin-exotic state, it can be well-accessed by the $b_1 \times \nabla$ operator that does not contain an explicit chromo-magnetic field. However, ∇ contains a link variable and may allow for a gluonic excitation. The quality of the effective masses arising from the $b_1 \times \nabla$ operator is not high, but the fit yields reasonable errors. The two lowest lying states are very close. In fact, within their errors the effective masses are overlapping so that in the statistical analysis it was necessary to sort the jackknifes according to the proximity of the eigenvectors to the ones obtained on the original ensemble. This may hint at a hybrid nature of this channel. Static hybrid potentials are repulsive at short distances so that, within a potential model, we may expect smaller energy gaps between radial excitations [71–73].

The computed spectrum is displayed in Fig. 11, together with the experimental values.[5] We have used the spin-averaged $1\bar{S}$ mass Eq. (1) to fix the charm quark mass. The other states are predictions. Note, however, that we underestimated $m_{1\bar{S}}$ by about 15 MeV. The main effect of this is that all the predictions should be shifted up by 15 MeV. Keeping this in mind, we observe all spin-

averaged states below threshold coming out in qualitative agreement with the experimental data [50]. We indicate the experimental $D\bar{D}$ and $D\bar{D}^{**}$ open charm thresholds as horizontal lines. Negative parity states cannot decay into $D\bar{D}$ and the $D\bar{D}^{**}$ threshold is believed to play a more prominent rôle in the decay of hybrid mesons than $D\bar{D}^*$.

The spin-averaged $1\bar{P}$-$1\bar{S}$ splitting is underestimated, relative to experiment while the $2\bar{S}$-$1\bar{S}$ splitting comes out right. There may be issues with the scale setting, due to the unrealistic sea quark content. We have also remarked in Sec. II A above that there are reasons to believe [48] that the lattice spacing should be set to $a^{-1} \approx 1.81$ GeV rather than to the $a^{-1} \approx 1.72$ GeV that we used. This change would bring the $1\bar{P}$-$1\bar{S}$ splitting in line with experiment but
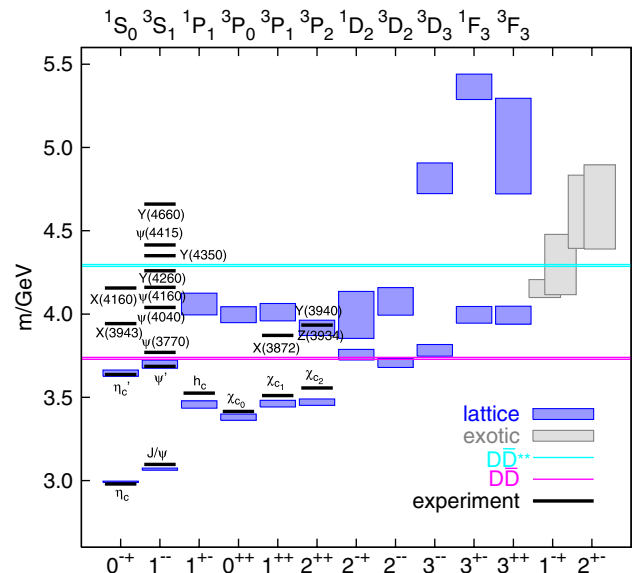

FIG. 11 (color online).   The predicted spectrum, together with the experimental values on ensemble (1); see Table I.

---

[5] In some cases, their J^{PC} assignment is still under debate. For instance, for the $X(3872)$ that we list as a 1^{++} state, a 2^{-+} assignment is not ruled out.

result in an overestimated $2\bar{S}$ mass. This, in turn, could then be due to a combination of finite size effects and interferences with the $D\bar{D}$ threshold in nature that do not occur on our ensemble, due to the heavy sea quark mass.

From potential NRQCD one would, to leading nontrivial order in $1/m_c$, expect the S-wave fine structure to be determined by the matrix element [74,75],

$$\frac{c_F^2}{3m_c^2}\langle\Psi|V_4(r)|\Psi\rangle, \tag{35}$$

where to leading order in perturbative QCD,

$$V_4(r) = \frac{32\pi}{3}\alpha_s\delta^3(r). \tag{36}$$

Ψ is the nonrelativistic charmonium wave function, α_s the strong coupling parameter and $c_F = 1 + \mathcal{O}(\alpha_s)$ is a matching coefficient that has only recently been determined in lattice schemes [76].

This illustrates the very short-distance nature of the S-wave fine structure that should be affected significantly both by lattice spacing effects and by differences in the running of the coupling depending on the sea quark content. It is also very sensitive to the charm quark mass. Reducing this by 5% would increase the splitting by 10%. So it is not surprising that we underestimate the experimental number of 117 MeV for the $1S$ fine structure splitting. We obtain $\Delta m_{1S} = m_{J/\Psi} - m_{\eta_c} = 77(2)$ MeV on ensemble (1), $\Delta m_{1S} = 88(4)$ MeV on ensemble (2), and $\Delta m_{1S} = 130(9)$ MeV on ensemble (3). Indeed, with lighter sea quark masses, this value increases.

For the $2S$ fine structure splitting, we obtain $\Delta m_{2S} = m_{\Psi(2S)} - m_{\eta_c'} = 54(6)$ MeV on ensemble (1) and $\Delta m_{2S} = 56(8)$ MeV on ensemble[6] (2), in agreement with the experimental value of 49(4) MeV. In view of the disagreement of the $1S$ splitting, this is quite surprising since one would have expected a lot of the systematics to cancel from the ratio of the $2S$ hyperfine splitting over the $1S$ splitting; see Eq. (35). We may therefore wonder whether either the physical η_c or the $\Psi(2S)$ states are unusually low, due to contributions from quark line disconnected diagrams. In the first case, our neglect of $\bar{c}c$ annihilation diagrams may be relevant while in the second case omitting $\bar{q}q$ creation (and the use of unphysically heavy light quark masses) would be the dominant effect(s); see Secs. IV and V below, respectively.

We remark that we also underestimate the P-wave fine structure. This is expected too and again mostly due to lattice spacing effects and an unrealistic sea quark content. We also notice that, in our approximation where the open charm thresholds are much higher than in nature, the $Z(3934)$ (recently renamed into $\chi_{c2}(2P)$ [50]) may indeed be associated with the χ_{c2}' state while the $X(3872)$ certainly

is lighter than one would have expected from an excited P-wave. However, in the first case, we cannot exclude the possibility that we have misidentified a 3^{++} state as 2^{++}, in particular, since this comes out lighter than the other two χ_c' multiplet masses. Finally, the proximity of the two 1^{-+} states as well as of the two 2^{+-} states may indicate a hybrid nature of these spin-exotic charmonia. We have not detected such indications in any of the other channels. With the exception of the A_2 ($J = 3$), in these cases the radial excitations are lower in energy than these spin-exotic states.

C. "Wave functions"

In Sec. II B, we have introduced couplings between an operator $\hat{O}_i$, $i = 1, \ldots, N$, and a physical state $|n\rangle$, $v_i^n = \langle 0|\hat{O}_i|n\rangle$. These will be approximated, up to a rotation and normalization; see below, by the $\psi^n(t, t_0)$ of Eq. (5). We employ the normalization, $\sum_i|\psi_i^n(t, t_0)|^2 = 1$. In the pseudoscalar channel, our operators read,

$$\hat{O}_i = \sum_{\mathbf{x},\mathbf{y}}\bar{c}(\mathbf{y})\Phi_i(\mathbf{y} - \mathbf{x})\gamma_5 c(\mathbf{x}). \tag{37}$$

Here Φ_i denotes the square of the Wuppertal smearing operator, Eq. (9), since we apply this to quark and antiquark fields. Φ_i is translationally invariant and will only depend on the difference $\mathbf{y} - \mathbf{x}$.

We employ a $N = 4$ dimensional trial basis consisting of $n_{\text{wup}} = 0, 5, 10$, and 40 iterations. This means that the Φ_i contain twice these numbers of iterations. Folding these smearing functions with the asymptotic eigenvectors results in a new smearing function,

$$\Psi^n(\mathbf{x}) = \sum_i\psi_i^n\tilde{\Phi}_i(\mathbf{x}), \tag{38}$$

where

$$\tilde{\Phi}_i = \frac{1}{d_i}\sum_j\Phi_j U_{ji}. \tag{39}$$

$U \in \text{SO}(N)$ diagonalizes $C(t_0)$ and $d_j > 0$ are the square roots of its eigenvalues,

$$[C^{-1/2}(t_0)C(t)C^{-1/2}(t_0)]_{ij} = \frac{[U^\dagger C(t)U]_{ij}}{d_i d_j}, \tag{40}$$

see Eq. (5). In particular, this means that the operators constructed from $\tilde{\Phi}_j$, $\hat{\tilde{O}}_j$ [see Eq. (37)] create states that are orthonormal at[7] $t = t_0$: $\langle\tilde{O}_i(t_0)\tilde{O}_j^\dagger(0)\rangle = \delta_{ij}$. Also note that if we neglect the coupling of the operator $\hat{O}_i$ to states with energies bigger than E_N, $d_i \propto \exp(-E_i t_0/2)$.

---

[6]On ensemble (3), where the radial excitations are seriously affected by the finite volume, we get $\Delta m_{2S} = 177(66)$ MeV.

[7]If corrections from truncating the basis can be neglected for $t_0 = 0$ (which is unlikely) then, at this t_0, $\psi_i^n \to v_i^n$ at large times t.

If we had perfect overlap with the respective physical states, then we could choose $t_0 = t = 0$. In this case, in the nonrelativistic limit, where we do not encounter particle-antiparticle creation, one may identify $|\Psi^{n\dagger}(\mathbf{x})\Psi^n(\mathbf{x})|$ with the quantum mechanical probability density. On a qualitative level, we may still think of $\Psi^n(\mathbf{x})$ as the wave function of the nth state. The used ensemble (1) is unfortunately too coarse to resolve the node structure of the gauge invariant $|\Psi^{n\dagger}\Psi^n|$. However, one can also plot a diagonal color component of $\Psi^n(\mathbf{x})$, after fixing to Coulomb gauge. In fact, the APE smeared gauge links are so close to unity that it is hard to resolve the differences between Coulomb gauge fixing and a nongauge fixed component from a plot.

In Fig. 12, we show a two-dimensional cross section of one color component of the normalized wave functions $\Psi^n(\mathbf{x})$, $n = 1, 2, 3$. In spite of the small basis and lattice volume, the node structure is consistent with the 1S, 2S, and 3S assignments, with no visible pollution from higher Fock states or D-waves. For the 1S "wave function" we obtain an rms radius, $\Delta r = \langle r \rangle_{\mathrm{rms}} = \sqrt{\sum_v r^2 |\Psi|^2} \approx 0.39$ fm. This compares reasonably well with the infinite volume continuum potential model expectation of about 0.4 fm [49].

D. Mixing in the vector channel

Because of its direct production in electron-positron annihilation, the vector channel is rich in experimentally confirmed resonances, as can be seen in Fig. 11. Of great interest is the inner structure of these states, in particular, of the $\Psi(2S)$ and the $\Psi(3770)$ states, which have a mass difference of only about 90 MeV and both are close to the $D\bar{D}$ open charm threshold. While J/Ψ is dominated by 1S quark-antiquark configurations, its excitations may exhibit a more complex structure.

As the name suggests, the $\Psi(2S)$ is thought to be a radial excitation. Since $\Psi(3770)$ is so close in mass, it is very improbable that it is excited in a further, higher radial vibration mode. One possibility, which we investigate here, is an orbital excitation where the quark-antiquark pair is in a relative D-wave. We start from an operator basis consisting of three S-wave and two D-wave interpolators,

$$(\bar{c}\gamma_i c)_0, \qquad (\bar{c}\gamma_i c)_{20}, \qquad (\bar{c}\gamma_i c)_{80},$$
$$(\bar{c}s_{ijk}\gamma_j D_k c)_0, \qquad (\bar{c}s_{ijk}\gamma_j D_k c)_{80}, \qquad (41)$$

where D_k is defined in Eq. (34) and $s_{ijk} = |\epsilon_{ijk}|$. The subscripts denote the numbers of smearing iterations, both for the quark and antiquark. Initially, we planned to include hybrid operators like $\bar{c}\gamma_5 B_i c$ into our basis but unfortunately these provided very poor signals throughout, independent of the smearing levels.

This mixing analysis is performed on ensemble (2); see Table I, with $t_0 = 3a$. We display the lowest four effective masses in Fig. 13. Indeed, the second and third eigenvalues
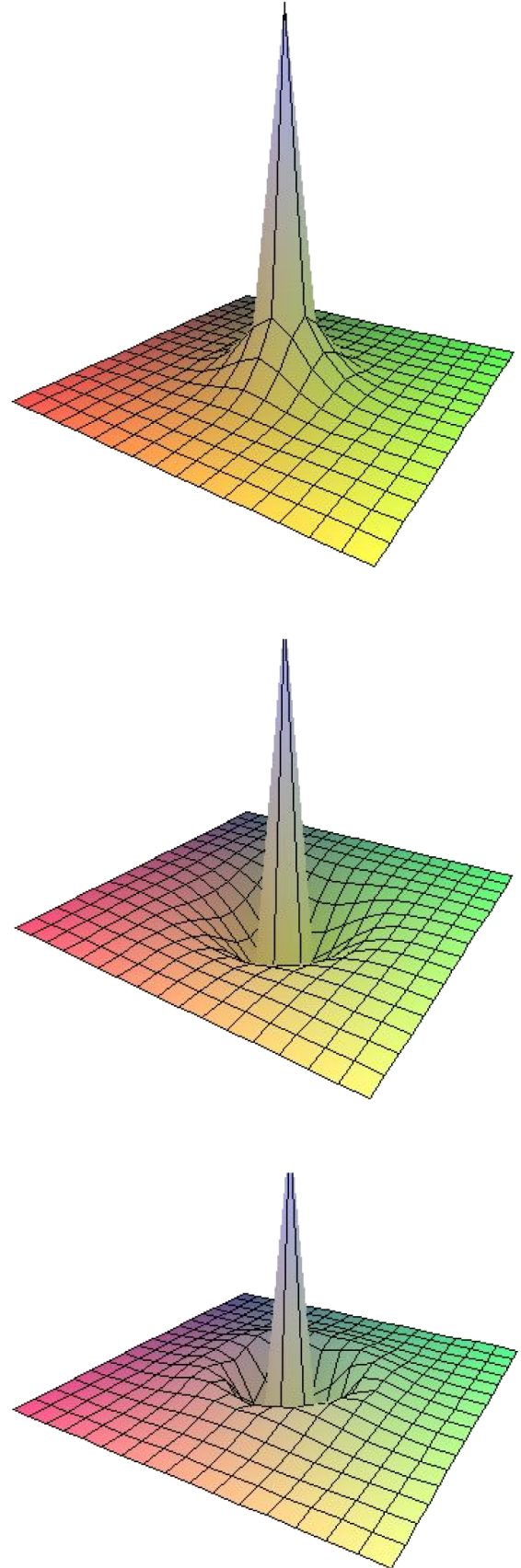

FIG. 12 (color online). The 1S, 2S, and 3S pseudoscalar wave functions.
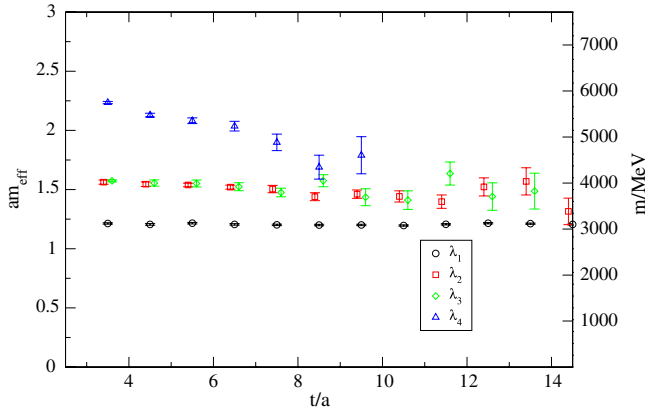
FIG. 13 (color online). Effective masses of the four lowest lying states in the vector channel on ensemble (2).

FIG. 14 (color online). Components of the first 1^{--} eigenvector; see Eq. (42).

lie very close. The fourth eigenvalue may be identified with the $\Psi(4040)$.

The eigenvector components reveal the overlaps between the trial operators and the physical eigenstates. The correlation matrix that is real in our case has the normalization ambiguity $C_{ij}(t) \mapsto e_i e_j C_{ij}(t)$, where $i = 1, \ldots, N$ and N is the dimension of the operator basis. One convenient choice is $C_{ii}(0) = 1$. The orthogonal transformation U that diagonalizes the correlation matrix at the time t_0 and the eigenvalues at this time d_i^2 of Eq. (40) depend on this initial normalization of $C(t)$. Following the discussion of Secs. II B and III C, see Eqs. (5) and (40), we can define effective overlaps,

$$v_i^n(t, t_0) = \left[\sum_k \left(\frac{\psi_k^n}{d_k}\right)^2\right]^{-1/2} \sum_j U_{ij} \frac{\psi_j^n(t, t_0)}{d_j}, \quad (42)$$

that in the limit $t_0 \gg 0$, $t \gg t_0$ will approach $v_i^n = \langle 0|\hat{O}_i|n\rangle$, up to an overall factor. The effective overlaps do not depend on the normalization choices e_i of $C_{ij}(t)$. Our normalization $\sum_i |v_i^n(t, t_0)|^2 = 1$ also implies $\sum_n |v_i^n(t, t_0)|^2 = 1$, which is equivalent to ignoring any effects of higher lying states. In Figs. 14–16, we display the first three $v_i^n(t, t_0 = 3a)$.

As one would expect the ground state, the J/Ψ, does not receive any contributions from the two D-wave operators. Interestingly, the second eigenstate, that is energetically very close to the third one (in fact for most t-values we can only differentiate between these states by tracing their eigenvector components), does not "see" any D-wave operators either. We remark that at the t-values where these second and third energy eigenvalues differ from each other we encounter more "mobility" of the eigenvector components; see Figs. 13, 15, and 16. Note the relative sign change in the case of the first excitation between the local/narrow and the wide operators, resulting in a node of the spatial wave function, similar to the $2S$ state of Fig. 12. This strongly suggests a $\Psi(2S)$ assignment for this state. Conversely, the third eigenvalue only couples to
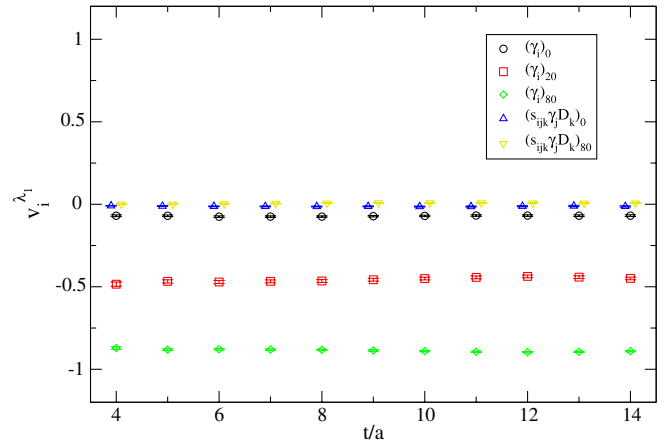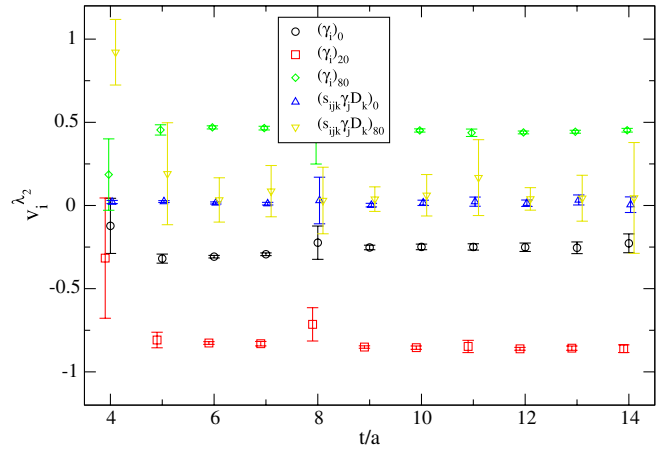

FIG. 15 (color online). Components of the second 1^{--} eigenvector.

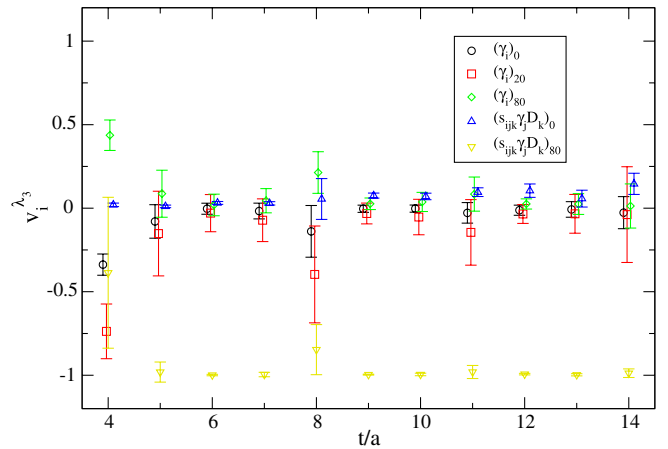
FIG. 16 (color online). Components of the third 1^{--} eigenvector.

the wide smeared D-wave operator, which obviously leaves it as a candidate for the $\Psi(3770)$. These results compare reasonably well with the ones of Ref. [70]. We conclude that the charm quark is sufficiently heavy for S- and D-waves to undergo only very mild mixing. So, at least for charmonia of masses below 3.8 GeV, it is meaningful to label states by their angular momenta. However, we have not yet considered the effect of open charm thresholds. We will address this question in Sec. V below.

IV. MIXING BETWEEN THE η_c AND THE LIGHT η MESON

Charmonia are flavor-singlet states, however, so far we have neglected the charm quark annihilation diagram that arises from Wick contracting the correlation function, $\langle[\bar{c}\Gamma c](t)[\bar{c}\Gamma c]^\dagger(0)\rangle$. The inclusion of quark line disconnected diagrams may affect charmonium masses. In particular, the proximity of the mass of the η_c meson to that of the pseudoscalar glueball, which may propagate as an intermediate state after $\bar{c}c$ annihilation, may have some effect [77]. This glueball mass was consistently determined in simulations of pure gauge theories on isotropic lattices to be [78] (2630 ± 290) MeV and on anisotropic lattices as[8] [79] (2637 ± 26) MeV. We also know that the light quark analogue of the η_c, the η' meson is much heavier than the light octet pseudoscalar mesons, due to the $U_A(1)$ anomaly. Naturally, chiral symmetry will not play a prominent role for charm quarks. However, this does not exclude a remnant effect of the vacuum topology that may lift the η_c mass by a few MeV.

First, calculations of the disconnected contribution both with $n_F = 2$ sea quarks and in the quenched approximation are consistent with no mass shift of the η_c mass [80,81], within statistical errors of about 20 MeV. More recently, in the quenched approximation the η_c mass was estimated to increase by 1–2 MeV [82] due to disconnected diagrams and, including sea quarks, this effect may become 1–4 MeV [82].

Naturally, when sea quarks are included both physical eigenstates, the η_c and the η', will contain light as well as charm valence quarks. The charm-anticharm component will be dominant within the η_c while the η' will almost exclusively contain light quarks. In our case, we employ $n_F = 2$ sea quarks and therefore an isosinglet η state assumes the role of the η'. In addition, we have an isovector π triplet, instead of the octet. When the disconnected quark loop is included then, at large Euclidean times, the η_c state will decay to the ground state in the $J^{PC} = 0^{-+}$ channel, which is the η meson. The physical η_c will only appear within the tower of excitations of this ground state. Following Ref. [42], we call this effect "implicit" mixing: the $\bar{c}\gamma_5 c$ state already intrinsically contains
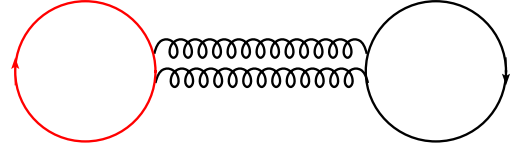

FIG. 17 (color online).   The lowest order perturbative QCD graph responsible for the mixing between $\bar{c}\gamma_5 c$ and $\bar{q}\gamma_5 q$ states. The red lines correspond to charm quarks, the black ones to light quarks, the twiddly ones to gluons.

a $\bar{q}\gamma_5 q$ contribution. However, one would expect the coupling of the $\bar{c}\gamma_5 c$ creation operator to this state to be very weak. Otherwise, charmonia would not be stable in nature either. This means that we can treat this as a perturbation. We decompose the physical Hamiltonian $H = H_0 + \lambda H_1 + \cdots$, into a part H_0 with[9] $\bar{c}c$ and $\bar{q}q$ eigenstates, without pair creation. The small perturbation λH_1 is then responsible for the mixing. Neglecting radial, gluonic, or multiquark excitations, the physical η_c wave function of this two-state system reads, to first order in the small parameter λ,

$$|\eta_c\rangle = |\bar{c}c\rangle + \lambda \frac{\langle \bar{q}q|H_1|\bar{c}c\rangle}{E_{\bar{c}c} - E_{\bar{q}q}}|\bar{q}q\rangle. \tag{43}$$

While we do not know the functional form of H_1 or of the unperturbed wave functions, we can evaluate all the relevant matrix elements on the lattice. Figure 17 depicts the graph responsible for this mixing to lowest order in perturbative QCD.

Obviously, the mixing will depend on the light quark mass value m_q. With decreasing m_q, the denominator of Eq. (43) will become larger. However, we would also expect the matrix element in the numerator to increase since the probability of creating a light quark-antiquark pair may increase with decreasing quark mass. Thus, ideally one would realize several light quark masses to clarify this issue.

Similar to our investigation of mixing in the vector channel of Sec. III D, we also calculate a correlation matrix here. We choose the basis states,

$$\begin{array}{ccc}
(\bar{c}\gamma_5 c)_0, & (\bar{c}\gamma_5 c)_{10} & (\bar{c}\gamma_5 c)_{80}, \\
(\bar{q}\gamma_5 q)_0, & (\bar{q}\gamma_5 q)_5 & (\bar{q}\gamma_5 q)_{40}, \tag{44}
\end{array}$$

where the subscripts denote the number of Wuppertal smearing iterations. The diagonalization of this matrix at large times will not only allow us to extract the energy levels, but it will also provide us with qualitative information on the charm and light quark content of the physical states. In Fig. 18, we sketch the structure of the mixing matrix between the $\bar{c}c$ and $\bar{q}q$ sectors, omitting the different smearing levels. Red lines represent charm quark propagators and blue lines light quark propagators. The

---

[8]We converted the numbers into units of $r_0 = 0.467$ fm and ignore the uncertainty in this scale setting.
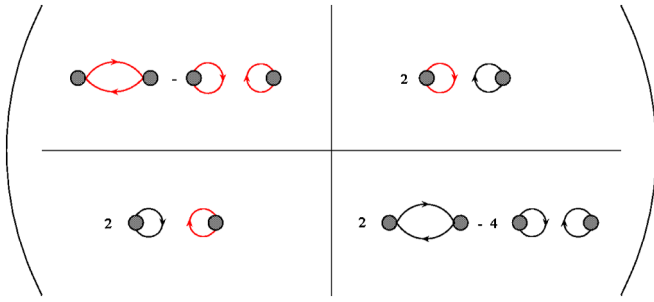
[9]We omit the Γ structure for convenience.

FIG. 18 (color online). Correlation matrix for the mixing between states created by $\bar{c}\gamma_5 c$ and by $\bar{q}\gamma_5 q$ operators. Red (gray) lines represent charm quarks, black lines light quarks.

FIG. 20 (color online). Effective masses from the eigenvalues of the full matrix. As a reference point, the effective masses from the (unmixed) submatrices are plotted too (black squares).

prefactors are due to the $n_F = 2$ mass degenerate sea quark flavors. The upper left corner contains the $\bar{c}c$ sector, the lower right corner the $\bar{q}q$ sector. The off-diagonal elements quantify the mixing.

Note that already in the pure charmonium sector implicit mixing will occur, due to intermediate light quark loops in the disconnected part; see Fig. 19, or even intermediate glueball states. If the explicit mixing encoded in the $\mathcal{O}(\lambda)$ off-diagonal elements of the mixing matrix is small, then we will not be able to resolve the $\mathcal{O}(\lambda^2)$ decay of $\bar{c}c$ states into states dominated by $\bar{q}q$ within any sensible Euclidean time distances. This further justifies and motivates our mixing matrix approach.

Our strategy is as follows. We first determine the eigenvalues and eigenstates of the three by three submatrices within each of the flavor sectors, separately, in order to obtain an "unperturbed" approximation to the spectrum. We will then compare the spectrum and the eigenvector components of this reference point to the situation with the mixing elements switched on.

The all-to-all propagator estimates for both, the charm and light disconnected loops have been improved by HPE, obdSSP and color partitioning, see Sec. II E. For the light quark propagators, in addition the TSM [57,58] with $n_t = 25$ has been applied. We analyze ensemble (1), see Table I, with a pseudoscalar mass of about 1 GeV. At this heavy mass, we find an η-π mass splitting of only 52(13) MeV. Within the diagonal three-by-three submatrices, we find the disconnected charmonium loops to be very noisy. Since the statistical errors are bigger than the expected splitting of a few MeV, we ignore these contributions. If we were to

detect significant off-diagonal contributions to the full correlation matrix, then of course we would have to revisit this issue at a later stage.

The masses of the light η meson and of its first radial excitation[10] η' can be extracted from the largest two eigenvalues of the submatrix containing the light quark creation and annihilation operators while the η_c and η_c' masses can be approximated from the $\bar{c}c$ sector. We find a diagonalization of the full six-by-six matrix to be numerically unstable and hence restrict ourselves to the basis of the states $(\bar{c}\gamma_5 c)_{10}$, $(\bar{c}\gamma_5 c)_{80}$, $(\bar{q}\gamma_5 q)_5$, and $(\bar{q}\gamma_5 q)_{40}$ for our subsequent full-fledged mixing analysis.

In Fig. 20, we display the effective masses of the η, η', η_c, and η_c' states, with the off-diagonal matrix elements switched off (squares). These are compared to the lowest three effective masses obtained from the four-by-four matrix with the mixing switched on, as explained above. We shift the latter effective masses slightly to the right. No relevant deviations can be seen.

The mixing can be studied in more detail by investigating the respective effective eigenvector components that are defined in Eq. (42) where U diagonalizes $C(t_0)$ that has the eigenvalues d_i^2. We display these effective overlaps for the ground state η meson in Fig. 21 and for the η_c in Fig. 22. The fitted components are displayed in Table VII. Indeed, the η does not receive any statistically relevant $\bar{c}c$ contribution and vice versa. The summed probability to find the η meson in a state that can be created by the $\bar{c}c$ operators amounts to $(4 \pm 25) \cdot 10^{-4}$ and to find the η_c in a state created by $\bar{q}q$ to $(4 \pm 22) \cdot 10^{-4}$. These tiny upper limits on possible mixing effects also render a relevant coupling of the η_c state to the pseudoscalar glueball extremely unlikely since this glueball can appear as an intermediate state in diagrams of the type depicted in Fig. 17.
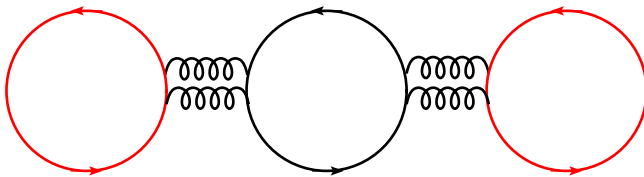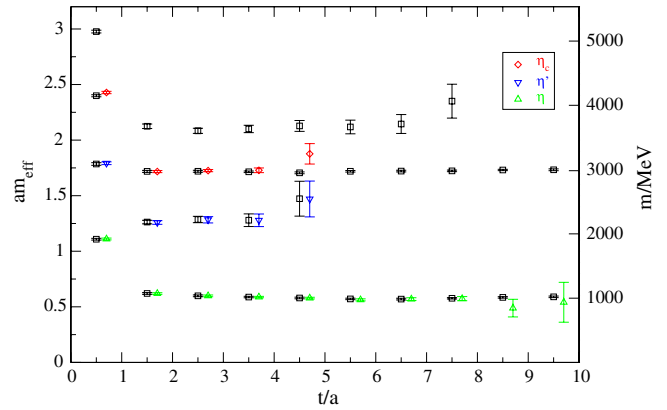

FIG. 19 (color online). The lowest order perturbative QCD graph responsible for implicit mixing between states created by $\bar{c}\gamma_5 c$ and by $\bar{q}\gamma_5 q$ operators.

---

[10]This should not be confused with the pseudoscalar flavor-singlet meson in the $n_F = 2 + 1$ theory.
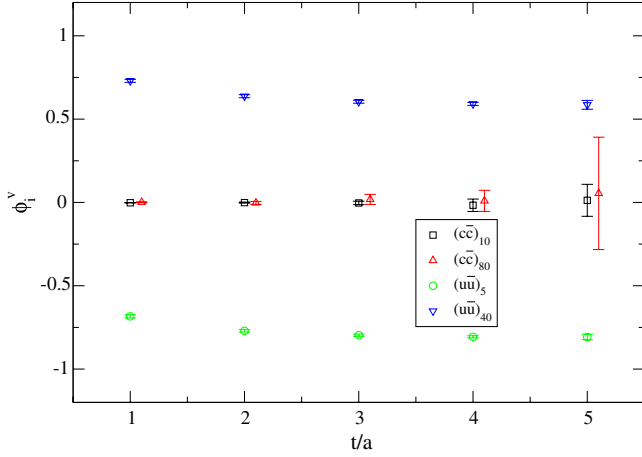
FIG. 21 (color online).   Eigenvector components of η in the full basis.
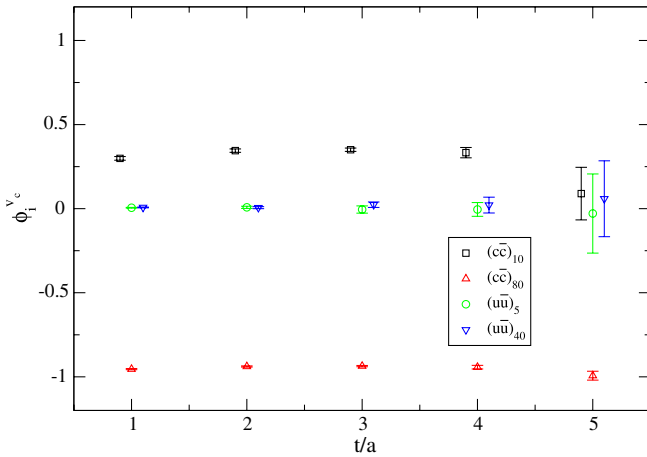

FIG. 22 (color online).   Eigenvector components of η_c in the full basis.

Obviously, the energy shift from explicitly admitting $\bar{c}c$ annihilation and light quark creation cannot significantly differ from zero either. We find a mass difference, $m_{\eta_c}^{\mathrm{mixed}} - m_{\eta_c}^{\mathrm{unmixed}} = 11(24)$ MeV. After this demonstration of the feasibility of such studies, we wish to further reduce the statistical errors and to vary the light quark mass in the near future. We address contributions from higher Fock states that may be relevant, e.g. for the η_c' state in the following section.

TABLE VII.   Fitted eigenvector components of the η and η_c states from the diagonalization of the full matrix.

	$(c\bar{c})_{10}$	$(c\bar{c})_{80}$	$(q\bar{q})_5$	$(q\bar{q})_{40}$
η	$-0.017(37)$	$0.009(63)$	$-0.806(1)$	$0.591(9)$
η_c	$0.333(30)$	$0.943(11)$	$0.000(41)$	$0.021(47)$

V. MIXING BETWEEN $\bar{c}c$ AND $D\bar{D}$ MOLECULAR OR TETRAQUARK STATES

Charmonia can decay into pairs of (excited) D and $\bar{D}$ mesons if their masses are above the allowed decay thresholds. Charmonia near these thresholds may, however, also contain significant Fock admixtures of $D\bar{D}$ molecules, see e.g. Ref. [83], or of $\bar{c}q\bar{q}c$ tetraquarks. We will study these effects in three different J^{PC} channels, 0^{-+}, 1^{--}, and 1^{++}. The first two channels are interesting with respect to the experimental overpopulation of the vector channel and the fact that the $\Psi(2S)$-η_c' fine structure splitting is very small, compared to that of the ground states; see the discussion of Secs. III B and IV above. The 1^{++} is phenomenologically relevant to disentangle the nature of the $X(3872)$ state.

We will address the question of higher Fock state contributions to the spectrum by creating and destroying states employing both, the $\bar{c}c$ operators corresponding to η_c, J/Ψ, and χ_{c1} charmonia as well as the four-quark operators corresponding to $D_1\bar{D}^*$ in $J = 0$, $D_1\bar{D}$, and $D^*\bar{D}$ molecules, respectively. The analysis method is exactly the same as outlined in Sec. IV. However, in the present situation, the dependence of the mixing strength of Eq. (43) (replacing $\bar{c}c \mapsto \bar{c}q\bar{q}c$, $\bar{q}q \mapsto \bar{c}c$) on the light quark mass is evident: again, with decreasing light quark masses the numerator is likely to increase, however, the denominator will decrease as the energy gaps between open charm states and the first radial charmonium excitations become smaller. Therefore, we analyze ensemble (3) (see Table I) that, with a light pseudoscalar mass of about 280 MeV, is closest to the physical point. Note that, with the product $m_{PS}L \approx 2.6$, this $L \approx 1.84$ fm lattice is quite small so that, in particular, for radial excitations we may expect significant finite size effects.

We start from a six-dimensional operator basis containing three $\bar{c}c$ and three molecular interpolators, differing by their Wuppertal smearing levels. We label these as p(oint), n(arrow), and w(ide). The generic form of the meson operators centered at the spacetime position x reads,

$$M_x = (\bar{c}\Gamma_M c)_x, \qquad (45)$$

where for readability we omit the smearing functions. Within the molecular operators, we allow for a spatial separation $\mathbf{r}$,

$$Y_x(\mathbf{r}) = \frac{1}{\sqrt{2}}[(\bar{q}\Gamma_Y^1 c)_x(\bar{c}\Gamma_Y^2 q)_{x+\mathbf{r}}$$
$$+ (-)^s(\bar{c}\Gamma_Y^1 q)_x(\bar{q}\Gamma_Y^2 c)_{x+\mathbf{r}}]. \qquad (46)$$

The Γ structures and $s \in \mathbb{N}_0$ values for the states of interest are displayed in Table VIII; see also Ref. [84]. Note that in this exploratory study we restrict ourselves to operators with molecular contractions and ignore the possibility of arranging the quarks into tetraquarklike $\bar{c}\bar{q}$ and qc diquark-antidiquark structures.

TABLE VIII. Γ structures of meson and molecule interpolating fields; see Eqs. (45) and (46).

J^{PC}	Γ_M	Γ_Y^1	Γ_Y^2	s
0^{-+}	γ_5	γ_i	$\gamma_i\gamma_5$	0
1^{--}	γ_i	γ_5	$\gamma_i\gamma_5$	1
1^{++}	$\gamma_i\gamma_5$	γ_5	γ_i	1

In Fig. 23, we sketch the structure of the mixing matrix. The different smearing levels are again omitted for clarity. Red lines represent charm quark propagators and blue lines light quark propagators. The prefactors are due to the $n_F = 2$ mass degenerate light sea quark flavors. The upper left corner contains the $\bar{c}c$, the lower right corner the molecular sector. The off-diagonal elements encode explicit mixing. In our calculation, we omit the charm annihilation diagrams of the second lines within each of the correlation matrix sectors; based on our experience of Sec. IV above, we deem these numerically irrelevant. A similar matrix was constructed, e.g. in Refs. [41,85] in order to investigate the ρ meson decay width and light tetraquark states, respectively. Note that all the depicted diagrams that include light quark propagators include more than one quark line contraction since for $\mathbf{r} \neq \mathbf{0}$ Eq. (46) contains two terms.

The spatial separation within the molecular operators was tuned to maximize the correlation function of the molecular sector. This led us to employ the on-axis separation $r = 4a \approx 0.3$ fm. After some experiments, we decided to employ point-to-all propagators for all diagrams, with the exception of the top right diagram within the molecule-to-molecule sector; see Fig. 23. This necessitates to implement a light all-to-all propagator at the sink. For this purpose, we generated the equivalent of 100 complex $\mathbb{Z}_2$ stochastic estimates, employing the obdSSP, HPE, and TSM methods.
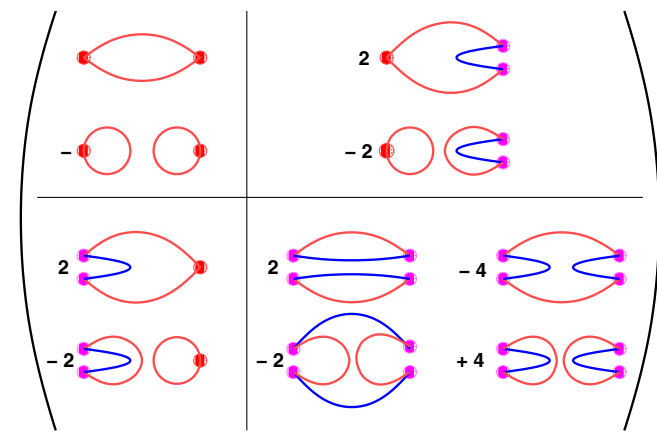

FIG. 23 (color online). Correlation matrix for the mixing of charmonia with $D\bar{D}$ molecules. Red (dark) lines represent charm quark propagators, blue (light) lines light quarks.
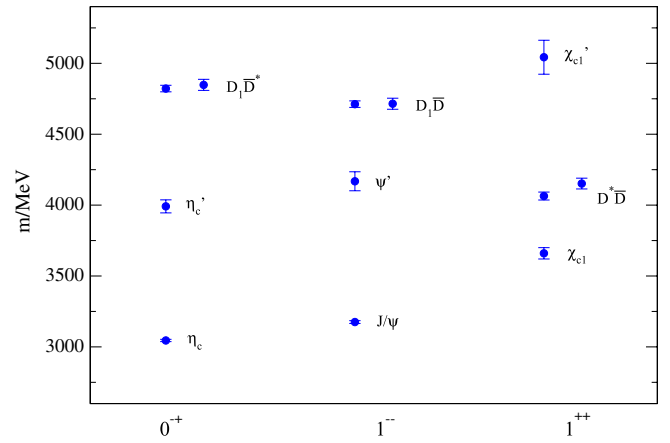

FIG. 24 (color online). Mass spectrum from separately diagonalizing the submatrices within the different sectors. The right points for the $D\bar{D}$ states correspond to the sums of noninteracting D mesons, the left points to interacting $I = 0$ D, and $\bar{D}$ mesons.

We first diagonalize the submatrices separately within the $\bar{c}c$ and molecular sectors to obtain a reference spectrum. This provides us with up to four reliable eigenvalues, two within each sector. However, the excited molecular channels are quite noisy so that in these cases we are only able to extract acceptable plateaus for the ground states. The remaining three states within each of the J^{PC} channels are plotted in Fig. 24. Next to the isospin[11] $I = 0$ molecular masses we also display the sums of the masses of the corresponding individual D and anti-D mesons. The resulting masses are also displayed in Table IX where the errors are statistical only. Because of the finite volume, the radially excited S-wave states are significantly higher than the corresponding experimental masses and the excited P-wave suffers even more from this effect, being by almost 1 GeV heavier than the corresponding $D^*\bar{D}$ molecule that is already heavier than in the real world due to the unphysically large light quark mass.

Within errors of about 30 MeV, we do not find any significant mass differences between molecules and their open charm constituent mesons in the pseudoscalar and vector channels. Of particular interest is the mass of the 1^{++} molecule that is by almost 200 MeV heavier than the $X(3872)$. However, this can easily be attributed to the light quark mass since the light pseudoscalar is still by 140 MeV heavier than the physical one. We find a significant binding of this axialvector molecule, $m_{D^*\bar{D}} - (m_{D^*} + m_D) = 88(26)$ MeV. There will be some volume and light quark mass dependence of this value that needs to be studied. Note that this binding energy is much bigger than the mass differences between the experimental $X(3872)$ of a fraction of an MeV with respect to electrically neutral open charm states and of a few MeV with respect to charged D and D^*

---

[11]Note that the $I = 1$ channel has been studied by Liu [86].

TABLE IX. Mass spectrum in MeV, neglecting the mixing between the two- and four-quark sectors.

$J^{PC} =$	0^{-+}	1^{--}	1^{++}
$\bar{c}c$ ground state	3045 (8)	3175(10)	3660 (40)
$\bar{c}c$ first excitation	3991(46)	4168(67)	5043(120)
$D_{(1)} + \bar{D}^{(*)}$	4848(39)	4715(39)	4152 (38)
$D_{(1)}\bar{D}^{(*)}$ molecule	4822(23)	4712(23)	4064 (28)

mesons. However, on a qualitative level, the increased attraction deserves some attention.

We base our fully fledged mixing study on a four-by-four submatrix with the operator basis M_p, M_n, Y_p, and Y_n. The normalization time is $t_0 = 2a$ for all channels. We start the discussion with the vector state and display the resulting lowest two effective masses, together with the unmixed reference masses in Fig. 25. The corresponding effective overlaps Eq. (42) are plotted in Fig. 26 for the J/Ψ and in Fig. 27 for the $D_1\bar{D}$ molecule. The J/Ψ receives the dominant contributions from the $\bar{c}c$ sector. However, the molecular configurations contribute significantly too. In contrast, the $D_1\bar{D}$ state only contains a small (but nonvanishing) $\bar{c}c$ admixture. This is very similar to the observation of Ref. [42] that the ground state potential between two static sources Q and $\bar{Q}$ receives a significant light quark contribution also for distances much smaller than the string breaking distance while its $\bar{Q}q\bar{q}Q$ excitation contains almost no $\bar{Q}Q$ component. We obtain the same qualitative picture for the pseudoscalar.

For the axialvector, the situation is different. We display the mixed and unmixed effective masses in Fig. 28. Note that in this case the mixed $D^*\bar{D}$ mass slightly increases, relative to the unmixed result. The corresponding effective overlaps are displayed in Figs. 29–31. The fitted results on the operator overlaps are summarized in Table X. The relative probability of creating the χ_{c1} by a four-quark

FIG. 26 (color online). Eigenvector components of J/Ψ in the full basis.

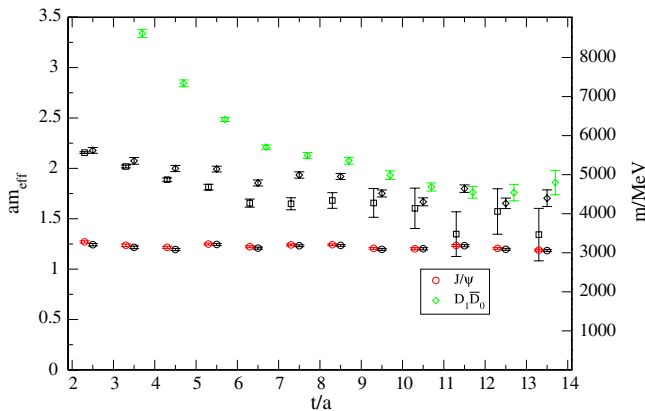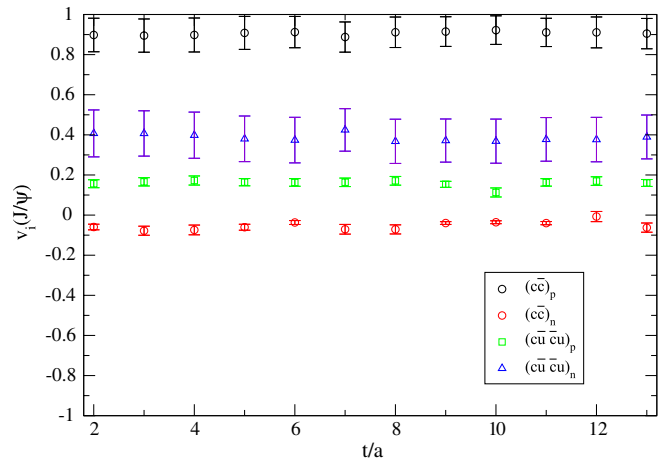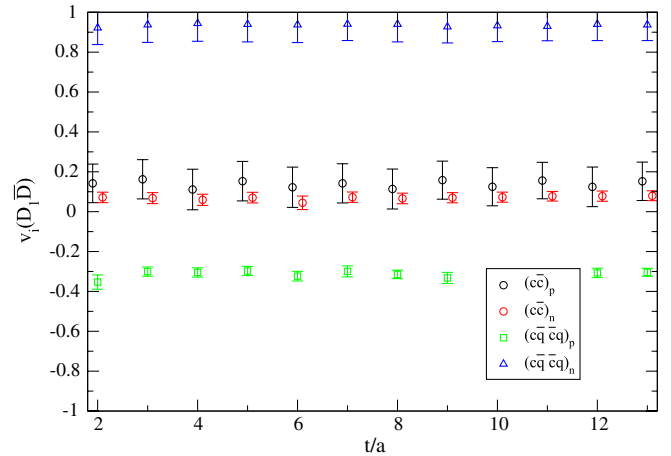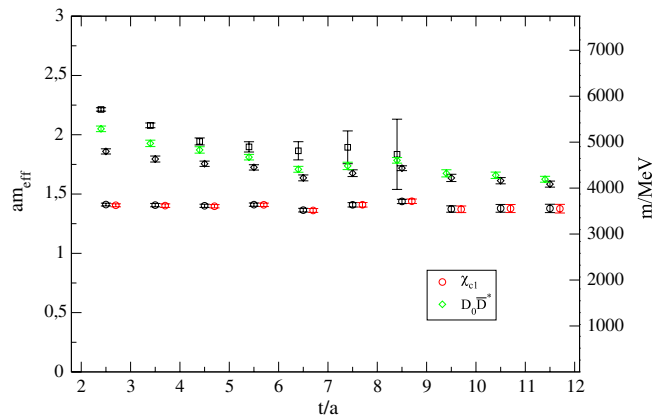FIG. 27 (color online). Eigenvector components of $D\bar{D}_1$ in the full basis.

FIG. 25 (color online). Effective masses from the eigenvalues of the full matrix in the 1^{--} channel. As a reference point, the effective masses from the submatrices are plotted too (black symbols).

FIG. 28 (color online). Effective masses of the eigenvalues of the full matrix in the 1^{++} channel. As a reference point, the effective masses from the submatrices are plotted too (black symbols).
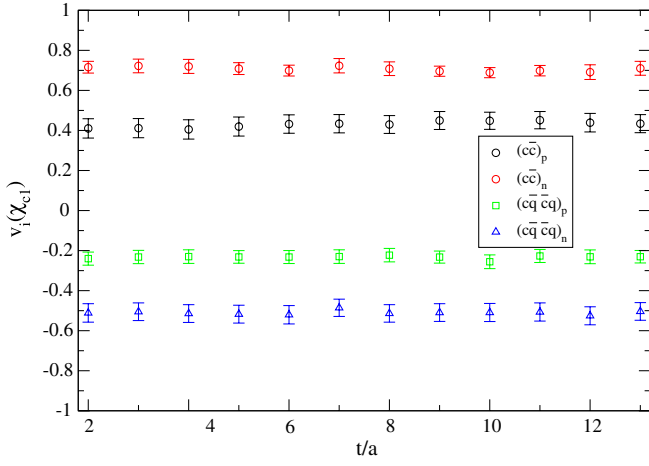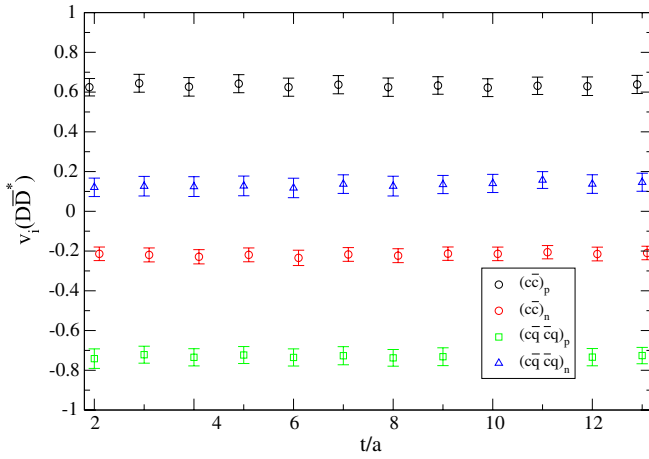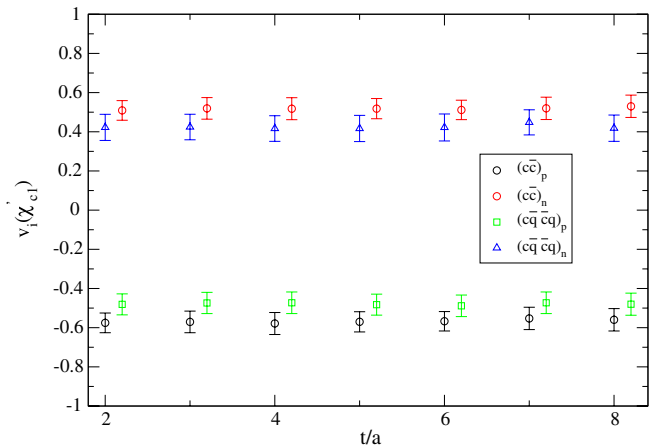
FIG. 29 (color online). Eigenvector components of χ_{c1} in the full basis.

FIG. 30 (color online). Eigenvector components of $D\bar{D}^*$ in the full basis.

FIG. 31 (color online). Eigenvector components of χ'_{c1} in the full basis.

TABLE X. Eigenvector components in the full basis.

	$(\bar{c}c)_p$	$(\bar{c}c)_n$	$(\bar{c}q\bar{q}c)_p$	$(\bar{c}q\bar{q}c)_n$
η_c	0.87 (5)	$-0.03(2)$	$-0.02(1)$	$-0.50(7)$
$D_1\bar{D}^*$	0.14 (2)	0.02(2)	$-0.95(15)$	0.29 (4)
J/Ψ	0.91 (7)	$-0.05(2)$	0.16 (2)	0.38(11)
$D_1\bar{D}$	0.14(11)	0.07 (2)	$-0.32(2)$	0.93 (8)
χ_{c1}	0.41 (4)	0.72 (3)	$-0.23(3)$	$-0.51(4)$
$D\bar{D}^*$	0.63 (4)	$-0.23(3)$	$-0.73(4)$	0.12 (3)
χ'_{c1}	$-0.55(6)$	0.53 (5)	$-0.49(5)$	0.41 (6)

operator is 0.29(5). For the first excitation that we identify as a $D^*\bar{D}$ molecule, it is 0.53(7), and for the χ'_{c1}, it is 0.36 (10): all these states appear to undergo strong mixing.

This casts doubt onto the validity of the mixing model Eq. (43). Setting this problem aside for the moment, we define unmixed χ_{c1} wave functions, projecting onto the $\bar{c}c$ components of the space spanned by our operator basis,

$$|\chi_{c1}\rangle^{\mathrm{un}} = d^{\chi_{c1}}_{(\bar{c}c)_p}|(\bar{c}c)_p\rangle + d^{\chi_{c1}}_{(\bar{c}c)_n}|(\bar{c}c)_n\rangle, \qquad (47)$$

and similarly for the excitation, χ'_{c1}, while for the $D^*\bar{D}$ state we can define the projection onto its four-quark components, $|D^*\bar{D}\rangle^{\mathrm{un}}$. Of physical interest are the overlaps between these idealized unmixed states and the respective physical states. These can be obtained by computing,

$$\langle D^*\bar{D}|\chi_{c1}\rangle^{\mathrm{un}} = d^{\chi_{c1}}_{(\bar{c}c)_p}d^{D^*\bar{D}}_{(\bar{c}c)_p} + d^{\chi_{c1}}_{(\bar{c}c)_n}d^{D^*\bar{D}}_{(\bar{c}c)_n}. \qquad (48)$$

The resulting probabilities read as follows,

$$\begin{aligned} |\langle D^*\bar{D}|\chi_{c1}\rangle^{\mathrm{un}}|^2 &= 0.01(1), \\ |\langle \chi_{c1}|D^*\bar{D}\rangle^{\mathrm{un}}|^2 &= 0.01(1), \\ |\langle \chi'_{c1}|\chi_{c1}\rangle^{\mathrm{un}}|^2 = |\langle \chi_{c1}|\chi'_{c1}\rangle^{\mathrm{un}}|^2 &= 0.01(1), \\ |\langle D^*\bar{D}|\chi'_{c1}\rangle^{\mathrm{un}}|^2 &= 0.22(5), \\ |\langle \chi_{c1}|D^*\bar{D}\rangle^{\mathrm{un}}|^2 &= 0.41(7) \end{aligned} \qquad (49)$$

while for the normalizations we obtain,

$$\begin{aligned} |\langle \chi_{c1}|\chi_{c1}\rangle^{\mathrm{un}}|^2 &= 0.47(7), \\ |\langle D^*\bar{D}|D^*\bar{D}\rangle^{\mathrm{un}}|^2 &= 0.30(6), \\ |\langle \chi'_{c1}|\chi'_{c1}\rangle^{\mathrm{un}}|^2 &= 0.34(5). \end{aligned} \qquad (50)$$

Because of cancellations, the ground state axialvector charmonium does not actively participate in the mixing while the radial excitation and the molecular state strongly mix with each other. However, the truncation of the mixing model at $\mathcal{O}(\lambda)$ is only justifiable on a qualitative level, as is obvious from $|\langle \chi_{c1}|\chi_{c1}\rangle^{\mathrm{un}}|^2 < 1$.

VI. SUMMARY AND OUTLOOK

We introduced the tools necessary to study the mixing of standard charmonium states with states created by four-quark operators and with light quark flavor-singlet states.

Of particular importance was the use of the variational generalized eigenvalue method as well as of improved stochastic all-to-all propagator methods. We introduced the staggered spin partitioning (SSP) and the recursive noise subtraction (RNS) methods (see also Ref. [44]). We also made use of the hopping parameter expansion (HPE) subtraction method [56] and of the truncated solver method (TSM) [57,58].

Our spin-averaged charmonium spectrum agrees fairly well with the experimental data. However, due to our unphysically heavy sea quark masses with light pseudo-scalar masses ranging from 1 GeV down to 280 MeV, due to the fact that we are simulating with $n_F = 2$ sea quarks only, and possibly due to the use of somewhat coarse lattice spacings of $a \approx 0.115$ fm and $a \approx 0.077$ fm, we significantly underestimate fine structure splittings. The ratio of the $2S$ fine structure splitting over the $1S$ splitting from which we expect some of the systematics to cancel comes out significantly larger than in experiment. One reason may be a distortion of the radial excitations due to their proximity to open charm thresholds, which lie higher in our simulations than in the real world.

The lowest spin-exotic state is a 1^{-+} vector with a mass of 4.15(5) GeV where the error is statistical only. The next highest such state can be found at 4.61(22) GeV with quantum numbers 2^{+-}. We interpret the small mass differences that we find with respect to radial excitations in these sectors as evidence of a charm-anticharm-gluon hybrid nature of these states. In other J^{PC} sectors, we do not see such evidence. At least for masses below 3.8 GeV, we do not detect any mixing between S- and D-waves, indicating that L is a relatively good quantum number for this mass range. This conclusion is also supported by examining the spatial structure of the optimized creation operators that we employ.

We realize that, to exclude mass shifts that are due to the flavor-singlet nature of charmonium states, it is not sufficient just to incorporate quark line disconnected charm annihilation diagrams, but that we also have to consider mixing with light flavor-singlet states. However, within errors of less than one per mille, we do not detect any light quark contributions to charmonium wave functions and vice versa. Moreover, within statistical errors of 24 MeV, we do not find any significant mass shift: $m_{\eta_c}^{\text{mixed}} - m_{\eta_c}^{\text{unmixed}} = 11(24)$ MeV. Clearly, in future studies we will aim at reducing this error.

We then moved on to investigate the binding between pairs of D and anti-D mesons in the pseudoscalar, vector, and axialvector sectors. Only the axialvector channel was clearly attractive, however, we emphasize that the volume scaling still needs to be investigated for definite conclusions. Subsequently, the mixing between isoscalar charmonium states created by two- and four-quark operators was investigated. Within the vector and pseudoscalar sector, at a light quark mass value that is 4 times as large as the physical one, these effects exist, but they are small. However, in the axialvector channel, the state that is dominated by the radial charmonium excitation strongly couples to the $D^*\bar{D}$ molecular state and vice versa. This is very interesting in view of the nature of the experimental $X(3872)$ state.

We plan to apply the methods that we developed and tested here in high precision studies of charmonium states with $n_F = 2 + 1$ sea quarks of different masses on various volumes and lattice spacings, within a large collaboration. First results of these systematic investigations were presented at the Lattice 2011 conference [37].

ACKNOWLEDGMENTS

[1] M. F. M. Lutz *et al.* (PANDA Collaboration), arXiv:0903.3905; I. Lehmann (PANDA Collaboration), Nucl. Phys. **A827**, 377 (2009).

[2] N. Brambilla *et al.* (Quarkonium Working Group), Eur. Phys. J. C **71**, 1534 (2011).

[3] E. Braaten, in *Proceedings of Continuous Advances in QCD, Minneapolis*, edited by M. Peloso (World Scientific, Singapore, 2008), p. 59.

[4] S. Godfrey and S. L. Olsen, Annu. Rev. Nucl. Part. Sci. **58**, 51 (2008).

[5] T. Barnes, J. Phys. Conf. Ser. **69**, 012004 (2007).

[6] M. B. Voloshin, Prog. Part. Nucl. Phys. **61**, 455 (2008).

[7] E. Eichten, S. Godfrey, H. Mahlke, and J. L. Rosner, Rev. Mod. Phys. **80**, 1161 (2008).

[8] E. S. Swanson, Phys. Rep. **429**, 243 (2006).

[9] A. De Rujula, H. Georgi, and S. L. Glashow, Phys. Rev. Lett. **38**, 317 (1977).

[10] V. A. Novikov, L. B. Okun, M. A. Shifman, A. I. Vainshtein, M. B. Voloshin, and V. I. Zakharov, Phys. Rep. **41**, 1 (1978).

[11] N. A. Törnqvist, Z. Phys. C **61**, 525 (1994).

[12] F. Close, C. Downum, and C. E. Thomas, Phys. Rev. D **81**, 074033 (2010).

[13] E. Oset, D. Gamermann, R. Molina, J. M. Nieves, E. R. Arriola, T. Branz, and W. H. Liang, in Charm2010 Workshop, Beijing, 2010 (arXiv:1101.2071).

[14] R. L. Jaffe, Phys. Rev. D **15**, 267 (1977).

[15] J. D. Weinstein and N. Isgur, Phys. Rev. Lett. **48**, 659 (1982).

[16] A. V. Manohar and M. B. Wise, Nucl. Phys. **B399**, 17 (1993).

[17] L. Maiani, F. Piccinini, A. D. Polosa, and V. Riquer, Phys. Rev. D **71**, 014028 (2005).

[18] L. Maiani, A. D. Polosa, and V. Riquer, Phys. Rev. Lett. **99**, 182003 (2007).

[19] T. Barnes, Nucl. Phys. **B158**, 171 (1979).

[20] T. Barnes and F. E. Close, Phys. Lett. **116B**, 365 (1982).

[21] M. S. Chanowitz and S. R. Sharpe, Nucl. Phys. **B222**, 211 (1983).

[22] N. Isgur, R. Kokoski, and J. E. Paton, Phys. Rev. Lett. **54**, 869 (1985).

[23] M. B. Voloshin and L. B. Okun, JETP Lett. **23**, 333 (1976).

[24] S. Dubynskiy and M. B. Voloshin, Phys. Lett. B **666**, 344 (2008).

[25] G. P. Lepage, L. Magnea, C. Nakhleh, U. Magnea, and K. Hornbostel, Phys. Rev. D **46**, 4052 (1992).

[26] C. T. H. Davies, K. Hornbostel, A. Langnau, G. P. Lepage, A. Lidsey, J. Shigemitsu, and J. H. Sloan, Phys. Rev. D **50**, 6963 (1994).

[27] A. S. Kronfeld, Phys. Rev. D **62**, 014505 (2000).

[28] J. Harada, A. S. Kronfeld, H. Matsufuru, N. Nakajima, and T. Onogi, Phys. Rev. D **64**, 074501 (2001).

[29] T. Burch *et al.* (Fermilab Lattice and MILC Collaborations), Phys. Rev. D **81**, 034508 (2010).

[30] W. E. Caswell and G. P. Lepage, Phys. Lett. **167B**, 437 (1986).

[31] A. Pineda and J. Soto, Nucl. Phys. B, Proc. Suppl. **64**, 428 (1998).

[32] N. Brambilla, A. Pineda, J. Soto, and A. Vairo, Nucl. Phys. **B566**, 275 (2000).

[33] G. S. Bali, Int. J. Mod. Phys. A **21**, 5610 (2006).

[34] E. Follana, Q. Mason, C. T. H. Davies, K. Hornbostel, G. P. Lepage, J. Shigemitsu, H. Trottier, and K. Wong (HPQCD and UKQCD Collaborations), Phys. Rev. D **75**, 054502 (2007).

[35] Y. Namekawa *et al.* (PACS-CS Collaboration), Proc. Sci., LATTICE2008 (2008) 121 [arXiv:0810.2364].

[36] Y. Namekawa *et al.* (PACS-CS Collaboration), Phys. Rev. D **84**, 074505 (2011).

[37] P. Pérez-Rubio *et al.*, Proc. Sci., LATTICE2011 (2011) 135 [arXiv:1108.6147].

[38] S. M. Ryan (Hadron Spectrum Collaboration), Proc. Sci., LATTICE2010 (2010) 124.

[39] T.-W. Chiu and T.-H. Hsieh (TWQCD Collaboration), Phys. Rev. D **73**, 094510 (2006).

[40] T.-W. Chiu and T.-H. Hsieh (TWQCD Collaboration), Phys. Lett. B **646**, 95 (2007).

[41] S. Prelovšek, T. Draper, C. B. Lang, M. Limmer, K.-F. Liu, N. Mathur, and D. Mohler, Phys. Rev. D **82**, 094507 (2010).

[42] G. S. Bali, H. Neff, T. Düssel, T. Lippert, and K. Schilling (SESAM Collaboration), Phys. Rev. D **71**, 114513 (2005).

[43] C. Ehmann and G. S. Bali, Proc. Sci., LAT2007 (2007) 094 [arXiv:0710.0256].

[44] C. Ehmann and G. S. Bali, Proc. Sci., LATTICE2008 (2008) 114 [arXiv:0903.2947].

[45] G. S. Bali and C. Ehmann, Proc. Sci., LAT2009 (2009) 113 [arXiv:0911.1238].

[46] B. Sheikholeslami and R. Wohlert, Nucl. Phys. **B259**, 572 (1985).

[47] A. Ali Khan *et al.* (QCDSF and UKQCD Collaborations), Nucl. Phys. **B689**, 175 (2004).

[48] J. Najjar *et al.* (QCDSF Collaboration) (unpublished).

[49] G. S. Bali and P. A. Boyle, Phys. Rev. D **59**, 114504 (1999).

[50] K. Nakamura *et al.* (Particle Data Group Collaboration), J. Phys. G **37**, 075021 (2010).

[51] C. Michael, Nucl. Phys. **B259**, 58 (1985).

[52] M. Lüscher and U. Wolff, Nucl. Phys. **B339**, 222 (1990).

[53] B. Blossier, M. Della Morte, G. von Hippel, T. Mendes, and R. Sommer (ALPHA Collaboration), J. High Energy Phys. 04 (2009) 094.

[54] S. Güsken, Nucl. Phys. B, Proc. Suppl. **17**, 361 (1990).

[55] M. Falcioni, M. L. Paciello, G. Parisi, and B. Taglienti, Nucl. Phys. **B251**, 624 (1985).

[56] C. Thron, S. J. Dong, K.-F. Liu, and H. P. Ying, Phys. Rev. D **57**, 1642 (1998).

[57] S. Collins, G. S. Bali, and A. Schäfer, Proc. Sci., LAT2007 (2007) 141 [arXiv:0709.3217].

[58] G. S. Bali, S. Collins, and A. Schäfer, Comput. Phys. Commun. **181**, 1570 (2010).

[59] C. Alexandrou, K. Hadjiyiannakou, G. Koutsou, A. 'O Cais, and A. Strelchenko, arXiv:1108.2473.

[60] K. Bitar, A. D. Kennedy, R. Horsley, S. Meyer, and P. Rossi, Nucl. Phys. **B313**, 348 (1989).

[61] S. J. Dong and K.-F. Liu, Nucl. Phys. B, Proc. Suppl. **26**, 353 (1992).

[62] S. Bernardson, P. McCarty, and C. Thron, Comput. Phys. Commun. **78**, 256 (1994).

[63] J. Viehoff *et al.* (SESAM Collaboration), Nucl. Phys. B, Proc. Suppl. **63**, 269 (1998).

[64] W. Wilcox, in *Lecture Notes in Computational Science and Engineering Vol 15: Numerical Challenges in Lattice Quantum Chromodynamics*, edited by A. Frommer *et al.* (Springer, Berlin, 2000), p. 127–141.

[65] G. S. Bali, T. Düssel, T. Lippert, H. Neff, Z. Prkacin, and K. Schilling (SESAM Collaboration), Nucl. Phys. B, Proc. Suppl. **140**, 609 (2005).

[66] W. Wilcox, Nucl. Phys. B, Proc. Suppl. **83**, 834 (2000).

[67] N. Mathur and S. J. Dong, Nucl. Phys. B, Proc. Suppl. **119**, 401 (2003).

[68] M. Deka T. Streuer, T. Doi, S. J. Dong, T. Draper, K.-F. Liu, N. Mathur, and A. W. Thomas, Phys. Rev. D **79**, 094502 (2009).

[69] X. Liao and T. Manke, arXiv:hep-lat/0210030.

[70] J. J. Dudek, R. G. Edwards, N. Mathur, and D. G. Richards, Phys. Rev. D **77**, 034501 (2008).

[71] S. Perantonis and C. Michael, Nucl. Phys. **B347**, 854 (1990).

[72] S. Collins (UKQCD Collaboration), Nucl. Phys. B, Proc. Suppl. **63**, 335 (1998).

[73] K. J. Juge, J. Kuti, and C. J. Morningstar, Phys. Rev. Lett. **82**, 4400 (1999).

[74] G. S. Bali, Phys. Rep. **343**, 1 (2001).

[75] A. Pineda and A. Vairo, Phys. Rev. D **63**, 054007 (2001).

[76] T. C. Hammant, A. G. Hart, G. M. von Hippel, R. R. Horgan, and C. J. Monahan, Phys. Rev. Lett. **107**, 112002 (2011).

[77] T. Feldmann, Int. J. Mod. Phys. A **15**, 159 (2000).

[78] G. S. Bali, K. Schilling, A. Hulsebos, A. C. Irving, C. Michael, and P. W. Stephenson (UKQCD Collaboration), Phys. Lett. B **309**, 378 (1993).

[79] Y. Chen *et al.*, Phys. Rev. D **73**, 014516 (2006).

[80] C. McNeile and C. Michael (UKQCD Collaboration), Phys. Rev. D **70**, 034506 (2004).

[81] P. de Forcrand, M. García Pérez, H. Matsufuru, A. Nakamura, I. Pushkina, I.-O. Stamatescu, T. Takaishi, and T. Umeda (QCD-TARO Collaboration), J. High Energy Phys. 08 (2004) 004.

[82] L. Levkova and C. DeTar, Phys. Rev. D **83**, 074504 (2011).

[83] E. J. Eichten, K. Lane, and C. Quigg, Phys. Rev. D **73**, 014014 (2006); E. J. Eichten, K. Lane, and C. Quigg, *ibid.* **73**, 079903(E) (2006).

[84] T.-W. Chiu and T.-H. Hsieh (TWQCD Collaboration), Proc. Sci., LAT2006 (2007) 170 [arXiv:hep-lat/0612025].

[85] S. Aoki *et al.* (CP-PACS Collaboration), Phys. Rev. D **76**, 094506 (2007).

[86] L. Liu, Proc. Sci., LAT2009 (2009) 099.

[87] R. G. Edwards and B. Joó (SciDAC, LHP, and UKQCD Collaborations), Nucl. Phys. B, Proc. Suppl. **140**, 832 (2005); C. McClendon, Jlab Report No. JLAB-THY-01-29, 2001, http://www.jlab.org/~edwards/qcdapi/reports/dslash_p4.pdf; P. A. Boyle, 2005, http://www.ph.ed.ac.uk/~paboyle/bagel/Bagel.html.